









Publication Year	2023
Acceptance in OA @INAF	2023-07-06T12:38:51Z
Title	The Gaia-ESO survey: Placing constraints on the origin of r-process elements
Authors	VAN DER SWAELMEN, Mathieu Benoit Jean; Viscasillas Vázquez, C.; CESCUTTI, Gabriele; MAGRINI, Laura; CRISTALLO, Sergio; et al.
DOI	10.1051/0004-6361/202243764
Handle	http://hdl.handle.net/20.500.12386/34262
Journal	ASTRONOMY & ASTROPHYSICS
Number	670

The *Gaia*-ESO survey: Placing constraints on the origin of *r*-process elements

M. Van der Swaelmen¹, C. Viscasillas Vázquez², G. Cescutti^{3,4,5}, L. Magrini¹, S. Cristallo^{6,7}, D. Vescovi⁸, S. Randich¹, G. Tautvaišienė², V. Bagdonas², T. Bensby⁹, M. Bergemann^{10,11}, A. Bragaglia¹², A. Drazdauskas², F. Jiménez-Esteban¹³, G. Guiglion¹⁴, A. Korn¹⁵, T. Masseron^{16,17}, R. Minkevičiūtė², R. Smiljanic¹⁸, L. Spina¹⁹, E. Stonkutė², and S. Zaggia¹⁹

(Affiliations can be found after the references)

Received 12 April 2022 / Accepted 7 July 2022

ABSTRACT

Context. A renewed interest in the origin of *r*-process elements has been stimulated by the multi-messenger observation of the gravitational event GW170817, with the detection of both gravitational waves and electromagnetic waves corresponding to the merger of two neutron stars. Such a phenomenon has been proposed as one of the main sources of the *r*-process. However, the origin of the *r*-process elements at different metallicities is still under debate.

Aims. We aim at investigating the origin of the *r*-process elements in the Galactic thin-disc population.

Methods. From the sixth internal data release of the *Gaia*-ESO, we have collected a large sample of Milky Way (MW) thin- and thick-disc stars for which abundances of Eu, O, and Mg are available. The sample consists of members of 62 open clusters (OCs), located at a Galactocentric radius between ~ 5 kpc and ~ 20 kpc in the disc, in the metallicity range $[-0.5, 0.4]$, and covering an age interval from 0.1 to 7 Gy, and about 1300 Milky Way disc field stars in the metallicity range $[-1.5, 0.5]$. We compare the observations with the results of a chemical evolution model, in which we varied the nucleosynthesis sources for the three elements considered.

Results. Our main result is that Eu in the thin disc is predominantly produced by sources with short lifetimes, such as magneto-rotationally driven SNe. There is no strong evidence for additional sources at delayed times.

Conclusions. Our findings do not imply that there cannot be a contribution from mergers of neutron stars in other environments, as in the halo or in dwarf spheroidal galaxies, but such a contribution is not needed to explain Eu abundances at thin-disc metallicities.

Key words. Galaxy: abundances – Galaxy: disk – open clusters and associations: general – stars: abundances

1. Introduction

Most of the numerous chemical species that make up our Universe have been produced in stellar interiors through nuclear processes that occur until the very last stages of a star's life. Chemical elements are classified in broad families depending on the nuclear process(es) and production site(s) responsible for their production. For instance, oxygen, magnesium, silicon, and calcium are called α -elements¹ since they are obtained by successive captures of α nuclei. However, scrutiny shows that all of the aforementioned elements cannot be strictly treated as a whole, since O and Mg are produced in stars of different mass classes and in different stages of stellar evolution than Si and Ca (and Ti). This difference translates in different yields, and therefore in a different pattern of chemical enrichment.

Elements with more protons than the iron nucleus are mainly produced by neutron accretion onto pre-existing iron seeds. This accretion is defined as slow (*s*-process) or rapid (*r*-process), with respect to the β -decay timescale (Burbidge et al. 1957). The rapid neutron-capture process, which is responsible for about half of the production of the elements heavier than iron (see, e.g., Kajino et al. 2019; Cowan et al. 2021), is not yet fully understood, and an interdisciplinary analysis is needed to reach an adequate comprehension of all the facets of the issue. Such an

¹ Titanium is often included in the list since its abundance behaves similarly to an α -element, although its atomic number is not a multiple of four.

approach should take into account nuclear astrophysics, observational results from stellar spectroscopy, gravitational waves, short gamma-ray bursts (GRBs), and galaxy formation theories (see, e.g., Côté et al. 2019).

A renewed interest in the origin of *r*-process elements has been stimulated by the multi-messenger observation (detection of both gravitational waves and electromagnetic waves) of the gravitational event GW170817, corresponding to the merger of two neutron stars (NSM; Abbott et al. 2017; Kasen et al. 2017). The spectroscopic follow-up of the fading glow of the kilonova AT 2017gfo associated with this NSM showed that the radiation is powered by the radioactive decay of lanthanides. The modelling of the observed broad absorption features in the late-time spectra was shown to be compatible with bands of heavy *r*-process elements such as cesium and tellurium (Smartt et al. 2017). On the other hand, the multi-epoch analysis of the early spectra revealed the presence of Sr (Watson et al. 2019), indicating this element as a common by-product of such events (Perego et al. 2022), despite the fact that its production is mostly due to the *s*-process at solar metallicity (Prantzos et al. 2020). These studies have revived the interest in NSMs as credible production sites of *r*-process elements (Pian et al. 2017). However, numerous parameters controlling the production of *r*-process by NSMs are yet to be estimated: yields, time-delay, frequency, and merging rate (see, e.g., Vangioni et al. 2016; Ojima et al. 2018, for a discussion on the coalescence time).

If GW170817 is likely the first observation of in situ production of heavy elements by the r -process, it does not yet answer the question of the origin of r -elements. Several possible sites of production and physical mechanisms have been considered in recent decades (see [Kajino et al. 2019](#), and references therein for a complete review) and are still under study. Here we briefly recall the most popular ones²: *i*) neutrino-driven winds above proto-neutron stars in core-collapse supernovae (CCSNe), which is likely the site of production of the *weak* r -process and produces neutron rich nuclei up to about $A \sim 125$ ([Woosley et al. 1994](#)); *ii*) magnetic neutrino-driven wind, which provides a possible mechanism for nucleosynthesis of rare heavy elements ([Thompson 2018](#)); *iii*) shock-induced ejection of neutron-rich material in CCSNe with $M < 10 M_{\odot}$ ([Hillebrandt et al. 1984](#)); *iv*) compact-object binary mergers, which can involve two neutron-stars (NSM) or a neutron star and a black hole binary system (NS-BH; [Lattimer & Schramm 1974](#); [Rosswog 2005](#); [Goriely et al. 2011](#); [Korobkin et al. 2012](#)). In these systems, the ejected matter can be very neutron-rich and it can produce elements up to $A \sim 300$; *v*) a magneto-hydrodynamic jet (MHDJ) supernova model, in which magnetic turbulence launches neutron rich material into a jet, undergoing r -process nucleosynthesis ([Nishimura et al. 2006](#)); *vi*) collapsar (failed supernovae) might produce r -process through neutron-rich matter coming from the accretion disc and ejected into a relativistic jet along the polar axis ([Fujimoto et al. 2006](#)); *vii*) r -process from dark-matter-induced black hole collapse ([Bramante & Linden 2016](#)); *viii*) truncated tr -process from fallback supernovae, in which there is a first collapse forming a neutron star and a subsequent infall causing the formation of a black hole. The r -process is interrupted when the neutron star collapses to a black hole ([Famiano et al. 2008](#)). Moreover, the i -process (e.g., [Mishenina et al. 2015](#)), characterised by intermediate neutron densities ($n \approx 10^{14} - 10^{18} \text{ cm}^{-3}$) between those of the s - ($n \approx 10^6 - 10^{10} \text{ cm}^{-3}$) and r -process ($n > 10^{20} \text{ cm}^{-3}$; e.g., [Hempel et al. 2016](#)), may play a role in the formation of the elements heavier than iron in low-mass, low-metallicity asymptotic giant branch (AGB) stars.

What emerges from this long list of possible production sites is that the theoretical framework is extremely varied and complex, and strong observational constraints are needed in order to choose the dominant production scenarios. On the one hand, one of the most commonly adopted approaches for posing observational constraints on the r -process nucleosynthesis are spectroscopic observations of the metal-poor stars in the halo of our Galaxy. They can indeed be used to trace the r -process nucleosynthesis (see, e.g., [Frebel 2018](#); [Horowitz et al. 2019](#)), since the production of most neutron-capture elements is dominated by the r -process in the early stages of the formation of the Galaxy. The enhanced scatter of halo low-metallicity stars in the [Eu/H] versus the [Fe/H] plane, compared to the α /H versus [Fe/H] plane, is a hint that the production of Eu in the early epochs of Galactic evolution might have been more stochastic compared to the production of the α elements, which are mainly produced by CCSNe (see, e.g., [Cescutti et al. 2015](#)). On the other hand, spectroscopic observations of stellar populations in the thin and thick discs give us information about the contribution of the r -process in more recent times. However, starting at [Fe/H] > -1.5 , stars do not present only r -process enrichment, since the production of neutron-capture elements by the

s -process starts to widely contribute to their abundance pattern (see, e.g., [Gallino et al. 1998](#)). For this reason, the choice of chemical elements with a tiny production by the s -process, and therefore with a production still largely dominated by the r -process at solar metallicity, is preferred for probing the evolution of the r -process in the Milky Way (MW) discs. Europium is an ideal element in this respect since 95 % of Eu is predicted to be produced by the r -process at the time of the formation of the Solar System ([Prantzos et al. 2020](#)), given our knowledge of the s -process yields (see, e.g., [Cristallo et al. 2011, 2015](#); [Bisterzo et al. 2014](#); [Karakas & Lugaro 2016](#)) and of the possible role of the i -process (e.g., [Denissenkov et al. 2019](#)).

In this work, we use the data from the sixth data release (iDR6) of the *Gaia*-ESO survey ([Gilmore et al. 2012](#); [Randich et al. 2013](#)) to study the origin and the role of the r -process in the Milky Way discs, analysing abundances of both field and cluster stars. We consider the abundances of Pr, Nd, Mo, and Eu. Following [Prantzos et al. \(2020\)](#), the abundances of these elements had a strong to moderate contribution from the r -process when the Solar System formed: 95 % for Eu, 27 % for Mo, 47 % for Pr, and 39 % for Nd. Other elements are known to have a strong contribution from the r -process, such as Sm or Dy, but those elements could not be measured in the *Gaia*-ESO spectra. On the other hand, the production of elements such as Ba or La is dominated by the s -process (see, e.g., [Arlandini et al. \(1999\)](#) for their s -process percentages in the Sun, ranging from 81 to 92% for Ba and from 62 to 83% for La), and are therefore out of the scope of this work. We add to our analysis the abundance of Mg and O, elements mostly produced by CCSNe, which are useful comparisons for identifying the timescale of the r -process.

The paper is structured as follows: in Sect. 2 we describe the *Gaia*-ESO dataset, and the sample of open cluster (OC) stars and the sample of field stars adopted in the present work. In Sect. 3, we describe the Galactic chemical evolution (GCE) model and its assumptions. We present our results, both as a function of age and of metallicity, in Sect. 4. In Sect. 5 we discuss the implications of our results for the sites, mechanisms, and timescales of the r -process, providing our conclusions and summarising our results.

2. Data and sample selection

2.1. The *Gaia*-ESO survey

For this work, we used the sixth data release of the *Gaia*-ESO survey ([Gilmore et al. 2012](#); [Randich et al. 2013](#)), selecting the highest-resolution spectra obtained with UVES (resolving power $R = 47\,000$ and spectral range 480–680 nm). The data reduction and analysis was done within the *Gaia*-ESO consortium, which is organised in several working groups (WGs). The spectral analysis was performed with a multi-pipeline approach: different nodes analysed the same dataset, and their results are combined to produce a final set of parameters and abundances. The homogenisation process made use of calibrators (benchmark stars, open and globular clusters), selected following the calibration strategy described in [Pancino et al. \(2017\)](#). The analysis of the UVES data for FGK stars is described in [Smiljanic et al. \(2014\)](#), and can be summarised in the following steps: INAF-Arcetri took care of the data reduction, and the radial and rotational velocity determination ([Sacco et al. 2014](#)); reduced spectra were distributed by WG 11 to the analysis nodes, which performed their spectral analysis, providing stellar parameters; the nodes' stellar parameters were homogenised by WG 15, and then

² The literature on the r -process sites being very rich, we tried to quote in this introduction the early works for each investigated r -production site.

redistributed to the nodes for the elemental abundances (line by line); WG 11 homogenised and combined the line-by-line abundances, providing the final set of elemental abundances, which were finally validated and homogenised by WG 15. The recommended parameters and abundances were distributed in the iDR6 catalogue, internally to the *Gaia*-ESO consortium, and they are publicly available through the ESO portal. In this work, we use the atmospheric stellar parameters, such as effective temperature, T_{eff} , surface gravity, $\log g$, and metallicity³ $[\text{Fe}/\text{H}]$, and the abundances of four r -process and two α -elements.

One of the most important aspects of *Gaia*-ESO, compared to other spectroscopic surveys, is that it dedicated about 36% of its observing time to open star clusters. As it is well known, open clusters offer the unique advantage of allowing a more precise measurement of their ages and distances than isolated stars. Moreover, the observation of several members of the same cluster also provides reliable measurements of their chemical composition. We can therefore reasonably consider open clusters among the best tracers of the chemical evolution of our Galaxy. On the other hand, open star clusters, by their intrinsic characteristics, are limited in the age and metallicity ranges they span, being a thin-disc population. In this context, it is beneficial to complement the use of clusters with that of the field stars also studied by the *Gaia*-ESO, which reach older ages and lower metallicities, and whose abundances are on the same abundance scale as those of open clusters.

2.2. The open cluster sample

In this work, we use the 62 open clusters with age ≥ 100 My available in the *Gaia*-ESO iDR6. Not including the youngest clusters does not affect our approach based on chemical evolution, and it also eliminates problems related to the analysis of the youngest stars, whose abundances may be affected by several issues such as stellar activity (see, e.g., Spina et al. 2020; Baratella et al. 2020, 2021). For our sample clusters, we used the homogeneous age determination obtained in Cantat-Gaudin et al. (2020), using the second data release of *Gaia*. The $[\text{Fe}/\text{H}]$ are from Randich et al. (2022), except for the clusters not present in that work, which were calculated in this work.

The membership analysis was performed as by Viscasillas Vázquez et al. (2022, hereafter VV22). Figure 1 shows the distributions of the properties of the sample of 62 OCs: the Galactocentric distance R_{GC} , the age, and the metallicity $[\text{Fe}/\text{H}]$. The sample covers a wide range in R_{GC} , from about 5 to 20 kpc, in age, from 0.1 to 7 Gy, and in metallicity $[\text{Fe}/\text{H}]$, from -0.45 to 0.35. As explained in the following paragraphs, some clusters disappear from the analysis, depending on the availability of the abundances for oxygen, magnesium, and europium.

For any star, we removed the abundance of a given element if the uncertainty on the given abundance was ≥ 0.1 . We also removed the outliers from each cluster, adopting the same approach used in VV22, namely the interquartile range (IQR) method. This resulted in discarding 23 stars with Eu values out of the range of the other stars in the same cluster: 10 of them extremely rich and 13 extremely poor compared to the other member stars of their respective OCs (see Fig. A.1). These stars, listed in Table A.3, will be analysed in a future work. In particular, we would like to mention one of them: the star with

³ In this paper, we use metallicity and $[\text{M}/\text{H}]$, and iron abundance and $[\text{Fe}/\text{H}]$ as synonyms.

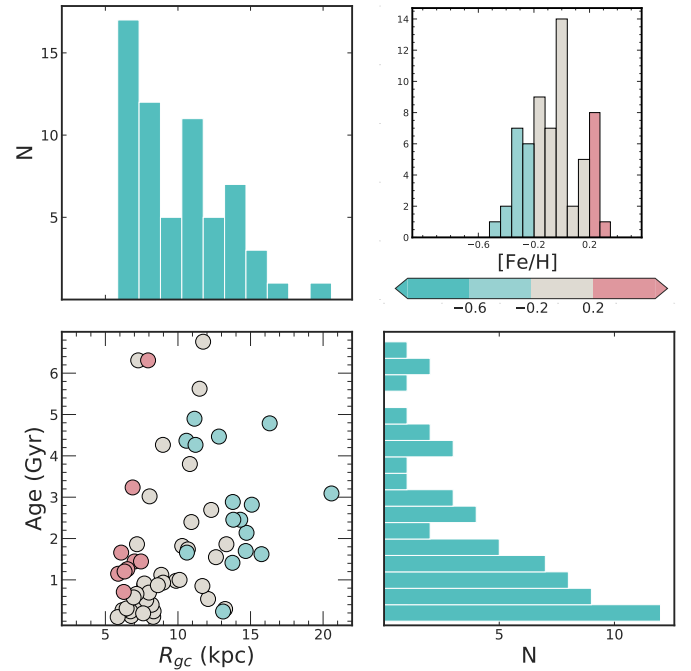


Fig. 1. Properties of our sample of 62 OCs. Upper left panel: histogram of R_{GC} . Lower left panel: distribution of clusters in the age vs. R_{GC} plane, colour-coded by $[\text{Fe}/\text{H}]$. Upper right panel: histogram of cluster metallicity. Lower right panel: histogram of the ages.

CNAME⁴ 06025078+1030280 in the open cluster NGC 2141 (or NGC 2141 4009) was already mentioned in VV22 for its extremely low abundance in all of its s -process elements, and now we recall it again for its low $A(\text{Eu})$ value.

After applying the selection cuts described above, the sample was reduced to 59 open clusters with Eu abundances, 62 OCs with Mg abundances, and 38 OCs with O abundances. The reason why fewer clusters have data for oxygen is that the only measured atomic line – the forbidden $[\text{O I}]$ at 6300 \AA – is a weak line, potentially contaminated by telluric lines (depending on the radial velocity of the star). No telluric correction has been performed by the *Gaia*-ESO data-reduction nodes, and therefore the forbidden O line shall be discarded when affected by the tellurics. In the case of a cluster, it means losing the whole set of member stars at a given epoch since all member stars have a similar radial velocity. We recall that the O line is also blended with an Ni line (Johansson et al. 2003) whose contribution is accounted for by means of line profile fitting (see Tautvaišienė 2015 for a description of the CNO determination method and see Fig. 6 in Bensby et al. 2004, highlighting how the contribution of the Ni blend changes with the star’s metallicity).

The Kiel diagram (KD) and the histograms of the distributions of the stellar parameters ($\log g$, T_{eff} , $[\text{Fe}/\text{H}]$) of member stars in the OC sample are shown in Fig. 2. The sample contains both dwarf and giant members, with a predominance of giants. The non-members are incorporated into our field-star sample.

In Tables A.1 and A.2, we provide the global metallicity of each cluster from Randich et al. (2022), together with the R_{GC} and age (Cantat-Gaudin et al. 2020), and the abundance ratios used along the paper with their σ . We provide both $[\text{E}/\text{H}]$ and $[\text{E}/\text{Fe}]$: the computation of the latter using the former is not straightforward since the reported overall

⁴ The CNAMEs reported throughout this publication are the IDs assigned by the *Gaia*-ESO survey.

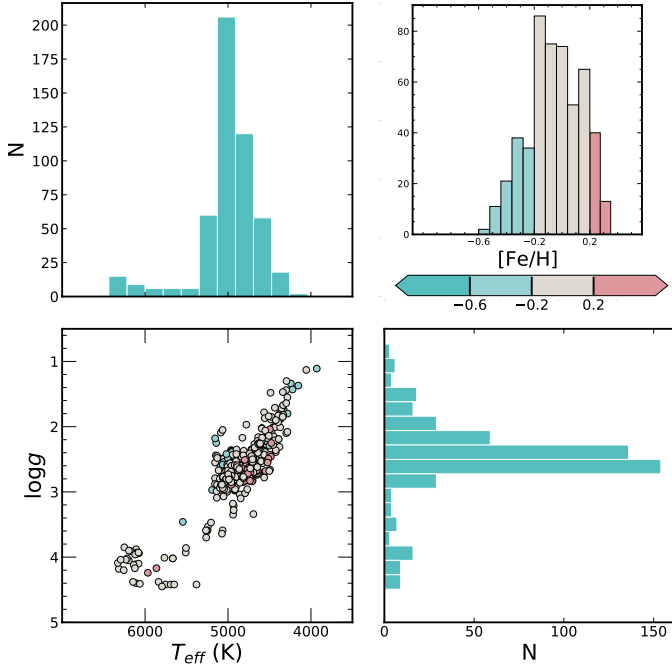


Fig. 2. Properties of the members of the OC sample. Upper left panel: histogram of T_{eff} . Lower left panel: Kiel diagram colour-coded by $[\text{Fe}/\text{H}]$. Upper right panel: histograms of $[\text{Fe}/\text{H}]$. Lower right panel: histogram of $\log g$.

metallicity $[\text{Fe}/\text{H}]$ is generally calculated with a larger number of members.

2.3. The field-star sample

The field-star sample is made up of stars whose ‘GES_TYPE’ header keyword of the spectra in the *Gaia*-ESO classification system corresponds to MW targets, which include halo, and thick- and thin-disc populations of the Milky Way. To that sample we also added benchmark stars (‘SD’) and the non-member stars of the OC sample (see above). We applied two quality cuts, the first one on the stellar parameters and on the signal-to-noise ratio (S/N): $S/N > 20$; $e[T_{\text{eff}}] \leq 150$ K, $e[\log g] \leq 0.25$, $e[[\text{Fe}/\text{H}]] < 0.20$, and $e[\xi] \leq 0.20$ km s⁻¹, and the second one on the abundances, considering only stars with $e[A(\text{El})] \leq 0.1$. We made a further selection, considering only the stars for which at least Eu II and an α -element (Mg I or O I) could be measured. This reduced the sample to ~ 1300 stars.

We did not apply to field stars any cut for possible outliers, which might indeed be stars of particular interest. However, we checked the barium and carbon content of our selection: we find a solar mean $[\text{Ba}/\text{Fe}]$ (standard deviation of ~ 0.1) and a slightly sub-solar $[\text{C}/\text{Fe}]$ (standard deviation of ~ 0.15). For both elements, 99% of the sample has $[\text{C}, \text{Ba}/\text{Fe}] \in [-0.2, 0.2]$, which is comparable to what is observed for the MW discs in other studies (e.g., with GALAH data, Buder et al. 2021). In addition, carbon-enhanced metal-poor stars (CEMPs) with possibly enhanced s - (e.g., Ba) or r - (e.g., Eu) abundances are not expected in the metallicity range of this study (see, e.g., Masseron et al. 2010; Goswami et al. 2021). Barium stars (main-sequence and red giant stars that have accreted the s -rich envelope of their former AGB companion, which is now an extinct white dwarf; e.g., Jorissen et al. 2019; Roriz et al. 2021) can be found at our metallicities but there is no sign of them from individual abundances,

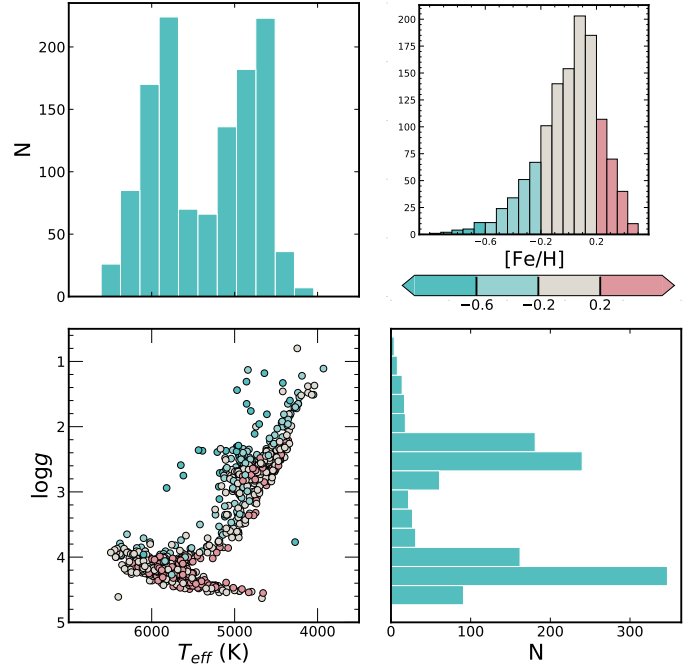


Fig. 3. Properties of the field-star sample. Definitions of the panels, symbols, and colours are the same as in Fig. 2.

as shown above (although the thresholds are not settled, mild Ba stars are expected to have $[\text{Ba}/\text{Fe}] \geq \sim 0.25$ and Ba stars often have $[\text{Ba}/\text{Fe}]$ ranging from 1 to 2). The KD and the distribution of stellar parameters of our sample of field stars are shown in Fig. 3. We computed the ages of the field stars, which are predominantly main-sequence stars at the turn off, using the AUSSIEQ2 tool, which is an extension of the qoyllur-quipu (Q2) PYTHON package (Ramírez et al. 2014). It calculates stellar ages by isochrone fitting, starting from the stellar parameters, and adopting a grid of isochrones. In the calculation, the code also takes into account the uncertainties on the stellar parameters.

2.4. The definition of the solar scale

In Table 1, we show the abundances of r -process-dominated and mixed elements, and of the two α elements, O and Mg, in the Sun (for *Gaia*-ESO iDR6 and from Grevesse et al. 2007) and in the open cluster M67 (mean values obtained for the whole sample of M67 member stars, and for giant and dwarf stars, separately). The cluster M67 indeed has a chemical composition very similar to the solar one (see, e.g., Önehag et al. 2011; Liu et al. 2016), and it is often used to normalise the abundances to the solar scale in samples containing both giant and dwarf stars (see, e.g., Magrini et al. 2018, VV22). The *Gaia*-ESO measurements for the solar abundances agree with those of Grevesse et al. (2007). The most discrepant element is Mo, but nevertheless it is in agreement within 2σ . The iDR6 abundances in the Sun and in M67 (mean value) are in agreement, within 1σ . Small differences can be appreciated between the average abundances for the M67 giants and the M67 dwarfs, particularly for Pr. Following VV22, we normalised the abundances of the dwarf and giant stars in our samples by the mean abundances of the M67 dwarf and M67 giant stars, respectively (we refer to VV22 for more details). For Mo, for which we have only abundances in the Sun and in the giants of M67, we used the former to normalise the abundances of dwarf stars, and the latter for the giant stars.

Table 1. iDR6 solar and M67 abundances for r -process elements and α -elements.

Species	Sun (iDR6)	Sun (Grevesse et al. 2007)	M67 (iDR6)	M67 (iDR6) (giants)	M67 (iDR6) (dwarfs)
O I	8.66±0.05	8.66±0.05	8.74±0.08	8.73±0.06	8.8±0.01
Mg I	7.51±0.02	7.53±0.09	7.50±0.05	7.53±0.04	7.49±0.04
Mo I	2.01±0.06	1.92±0.08	1.92±0.03	1.92±0.03	–
Pr II	0.57±0.02	0.58±0.10	0.57±0.07	0.54±0.03	0.61±0.04
Nd II	1.49±0.02	1.45±0.05	1.44±0.06	1.41±0.04	1.45±0.07
Eu II	0.52±0.02	0.52±0.06	0.54±0.11	0.56±0.08	0.53±0.11

3. The Galactic chemical evolution model

The chemical evolution model adopted is based on the two-infall model (Chiappini et al. 1997); there is a first and brief infall that mimics the formation of the thick-halo component, followed by a hiatus in the star formation and by a more extended infall, promoting the formation of the thin disc. Open clusters are formed during the second episode, and therefore a different modelling of the first infall should not change our results (see, for example, the recent paper by Spitoni et al. 2019). On the contrary, the inside-out formation of the Galactic disc plays a fundamental role, and for this we follow model B described in Chiappini et al. (2001), shown to be the best model in the comparison with Cepheids stars in Cescutti et al. (2007). As highlighted in Cescutti et al. (2007), the timescale of the enrichment dictates the steepness of the Galactocentric gradient for the chemical element. Flatter gradients are expected for elements produced on short timescales such as α -elements, which are produced by massive stars and ejected in the interstellar medium (ISM) by CCSNe on timescales of a few tens of million years (Woosley & Weaver 1995). On the other hand, elements produced mostly on longer timescales, for example iron, which is mostly produced by type Ia supernovae (SNe Ia; Nomoto et al. 1997), tend to present steeper gradients.

The original yields used for our simulations are based on the yields described in François et al. (2004) for oxygen, magnesium, and iron. These elements are produced by massive stars and SNe Ia. At the solar metallicity, most of the enrichment of magnesium and oxygen comes from massive stars; on the contrary, Fe is mostly produced by SNe Ia. For the europium yields, we assume two possible production modes in this work.

In the first model (model A), all the production takes place on a short timescale, and thus with no delay in the enrichment of the ISM. In particular, we considered the same yields for Eu adopted in Cescutti & Chiappini (2014), where the main producers were the magneto-rotationally driven (MRD) SNe (see Nishimura et al. 2015), so a yield of $1 \times 10^{-6} M_{\odot}$ per MRD SNe, assuming that only 10% of all the simulated massive stars explode as MRD SNe. This production is compatible with the enrichment by neutron star mergers having a short delay (Matteucci 2014; Cescutti et al. 2015).

We ran a second set of simulations (model B) with a second set of yields, where we considered the substantially increased production (a factor of five) of magnesium coming from SNe Ia. Since the model needs to respect the constraint dictated by the solar value, we had to decrease accordingly by a factor of 0.7 the yields for magnesium from CCSNe. The main consequence of this change was a larger fraction of magnesium produced on longer timescale. This had an impact on the chemical evolution trend of this element in the [Mg/Fe] versus [Fe/H]; the typical enhancement at a low metallicity is less pronounced and the

subsequent slope is also less steep. This possibility was already discussed in Magrini et al. (2017).

We also studied a model C, where the yields for magnesium produced by SNe Ia also have a metal dependency, which we impose empirically with this equation:

$$Y_{\text{Mg}}^{\text{SNeIa}} = 0.255 \frac{z}{z_{\odot}} [M_{\odot}] \quad (1)$$

With this metal dependency, the solar ring simulated by our GCE model is not expected to have significant variation; on the other hand, the outer rings tend to end their evolution with lower [Mg/Fe] compared to model B. In fact, due to the inside-out formation, the progenitors of SNe Ia present lower metallicity and this will inhibit the formation of Mg.

Finally, we ran a fourth model (model D) considering the enrichment of europium from both neutron star mergers and the same short timescale source as in the original set of yields. The original yields were evenly split between these two sources (50% from NSMs and 50% from MRD SNe); the magnesium yields were the same as model C. We do not show results assuming a single production for europium from NSMs since Côté et al. (2019) and Simonetti et al. (2019) have already proved this scenario not compatible with the chemical evolution of europium in the Galactic disc. We present the results with a fixed delay of 3 Gy since we have already introduced a degree of elaborateness with this double Eu production. In this way, we want also to produce results comparable to the model described in Skúladóttir & Salvadori (2020), with a similar delay time (4 Gy). The yields for each of these objects in our model is $1.5 \times 10^{-6} M_{\odot}$. The main assumptions of the four models for the yields of O, Mg and Eu are reported in Table 2.

4. Results

To investigate the origin of Eu in the Galactic disc, we compare its evolution with that of two α -elements that are expected to be mainly produced by CCSNe, on short timescales, namely Mg and O. The aim of our approach is to reveal possible differences in the production timescales of Eu with respect to the production timescales of these two α -elements, and to possibly highlight the need for a delayed nucleosynthetic channel for Eu, as expected by neutron star mergers (Korobkin et al. 2012). Although O and Mg are essentially produced by stars with masses in the same range, they are generated during different burning phases: oxygen is produced during the hydrostatic burning in the He-burning core and in the C shell, and it is expelled during the pre-supernova phase, while magnesium is produced during the hydrostatic burning in the C shell and in the explosive burning of Ne (see, e.g., Maeder & Meynet 2005). Therefore, we can expect differences in the evolution of these two

Table 2. Overview of the underlying assumptions for the production of O, Mg, and Eu for models A, B, C, and D.

Model	Source of oxygen	Source of magnesium	Source of europium
Model A	CCSNe	CCSNe (+ marginal contribution by SNe Ia)	MRD SNe
Model B	CCSNe	CCSNe (reduced) + SNe Ia (increased)	MRD SNe
Model C	CCSNe	CCSNe (reduced) + SNe Ia (increased and metal-dependent yields)	MRD SNe
Model D	CCSNe	CCSNe (+ marginal contribution by SNe Ia)	MRD SNe (50%) + NSMs (50%)

Notes. The words ‘increased’ and ‘reduced’ qualify the contribution of a given nucleosynthetic source, and should be understood as relative to the assumptions in model A.

elements. Moreover, for Mg, observational evidence has shown that the production from massive stars is not sufficient to explain its behaviour at a high metallicity. Several attempts have been made to explain the evolution of Mg, and its difference from that of oxygen, such as the use of metallicity-dependent yields of massive stars, the production from hypernovae at solar and/or higher than solar metallicity, larger contributions from SNe Ia, significant Mg synthesis in low- and intermediate-mass stars, or a mixture of all these production sites (see, e.g., Chiappini 2005; Romano et al. 2010; Magrini et al. 2017). As described in Sect. 3, to take into account the complexity of Mg production, we considered three different representations of the production of Mg: only CCSNe (model A), CCSNe and SNe Ia (model B), an CCSNe and metal-dependent SNe Ia production (model C). As for the Eu production, we investigated two scenarios: only MRD SNe (models A, B, and C), and an evenly mixed production by MRD SNe and NSMs (model D).

4.1. The evolution of Eu

Figure 4 shows the behaviour of Eu in the $[\text{Eu}/\text{Fe}]$ versus $[\text{Fe}/\text{H}]$ plane for the field-star sample (grey dots) and the open-cluster sample (coloured dots). For a metallicity lower than -0.8 , only a dozen of field stars outline the well-known plateau at $[\text{Eu}/\text{Fe}] \sim 0.4$, while at a larger metallicity, we note a decrease in $[\text{Eu}/\text{Fe}]$ with increasing $[\text{Fe}/\text{H}]$, reaching $[\text{Eu}/\text{Fe}] \sim -0.2$ at the super-solar metallicity $[\text{Fe}/\text{H}] \sim 0.4$. Over the metallicity range $[-0.4, 0.4]$, the distribution of the OC sample overlaps that of the field-stars sample and exhibits the same decrease. While the *Gaia*-ESO Mg abundances allow us to disentangle the thin- and thick-disc sequences in the $[\text{Mg}/\text{Fe}] - [\text{Fe}/\text{H}]$ plane, it is less obvious for Eu. However, as in Delgado Mena et al. (2017), and if we base our thin- and thick-disc separation on Mg, we note that (Mg-selected) thick-disc stars tend to have higher $[\text{Eu}/\text{Fe}]$ and lower $[\text{Fe}/\text{H}]$, while (Mg-selected) thin-disc stars tend to have solar $[\text{Eu}/\text{Fe}]$ and solar $[\text{Fe}/\text{H}]$. The fact that the frontier between the thin- and thick-disc sequences is blurred could be due to random errors in the measurements, keeping in mind that the Eu line is more difficult to measure than the Mg line. In addition, at the typical metallicity of the Galactic discs, we do not expect to detect the remnants of the stochastic enrichment of Eu, which are instead recognisable in the high $[\text{Eu}/\text{Fe}]$ spread in the low-density and low-metallicity halo environment for $[\text{Fe}/\text{H}] < -2.5$ (e.g., Cescutti et al. 2015; Naiman et al. 2018; Brauer et al. 2021). On the other hand, the OC sample defines a thinner sequence since, in a given metallicity bin, one finds only open clusters with a similar chemical history.

We also overplot the predicted evolution using our models C and D of $[\text{Eu}/\text{Fe}]$ with $[\text{Fe}/\text{H}]$ for the three radial rings defined for the OC sample, that is to say, for $R_{\text{GC}} = 4$ kpc (inner disc; blue curve), $7 \text{ kpc} \leq R_{\text{GC}} \leq 9$ kpc (solar ring; green curve) and $R_{\text{GC}} \geq 9$ kpc (outer disc; pink curve). While our solar-neighbourhood field-star sample shall be compared with

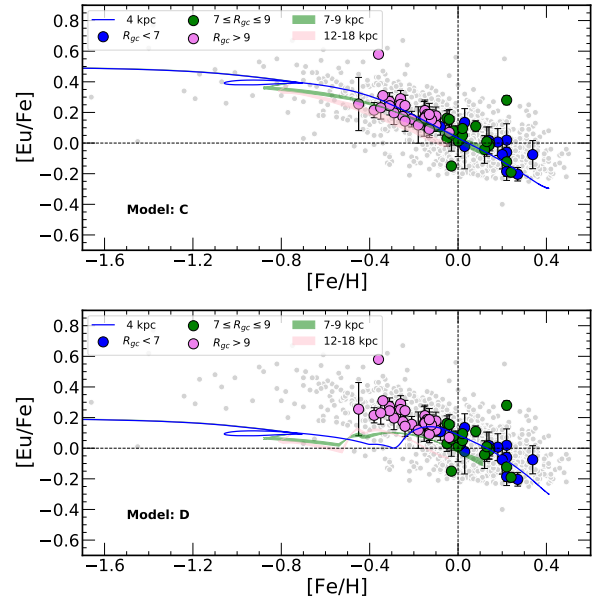


Fig. 4. $[\text{Eu}/\text{Fe}]$ vs. $[\text{Fe}/\text{H}]$ for the field-star sample and the OC sample. The data are colour-coded by Galactocentric bin, and compared with three curves of a given model, corresponding to the same radial regions and coloured in the same way as the data: inner disc (blue), solar-ring (green), and outer disc (pink). We report only models C and D, since the prescriptions for Eu in models A and B are the same as in model C. Small grey dots stand for the field-star sample. Top: comparison with model C. Bottom: comparison with model D. The error bars for the y-axis are displayed for the OC sample.

the solar-ring curves, a finer analysis must be adopted for our OC sample since open clusters in this study probe Galactocentric radii from 5 kpc to 20 kpc. Therefore, in the following sections, we compare the inner-disc curve to the inner OCs, the solar-ring curve to the solar-neighbourhood OCs, and the outer-disc curve to the outer OCs. Although we discuss four different models of chemical enrichment in this work, we recall here that the prescription for the Eu nucleosynthesis is identical in the three models A, B, and C (i.e. a rapid production of Eu by magneto-rotationally driven SNe), and only differs in model D, (i.e. a evenly mixed production of Eu by short-timescale MRD SNe and delayed NSMs).

For model C, the inner-disc and solar-ring curves overlap over the metallicity range $[-0.15, 0.15]$ and differ from each other at lower metallicities. The outer-disc curve gives lower $[\text{Eu}/\text{Fe}]$ ratios than the inner-disc and solar-ring curves at any metallicity over the metallicity range $[-0.8, 0]$, except at $[\text{Fe}/\text{H}] \sim -0.8$ where both the solar-ring and the outer-disc predictions yield $[\text{Eu}/\text{Fe}] \sim 0.4$. We note that the solar-ring curve is compatible with the mean trend of the field-star sample: it exhibits a flattening compatible with the plateau for $[\text{Fe}/\text{H}] \leq$

-0.8 and the slope of the decrease matches the observed one for $[\text{Fe}/\text{H}] \geq -0.8$. The overall shape of the predictions is also similar to the observed trends for the OC sample. While the solar-ring curve matches the observed ratios for the solar-neighbourhood OCs, the outer-disc and inner-disc curves are about 0.1 below the central trend but still agree at the 1σ level with the measured $[\text{Eu}/\text{Fe}]$.

For model D, the three curves exhibit a decrease in $[\text{Eu}/\text{Fe}]$ with metallicity until $[\text{Fe}/\text{H}] \sim -0.55$ for the outer-disc, and the solar-ring and $[\text{Fe}/\text{H}] \sim -0.3$ for the inner-disc, where a rapid increase in $[\text{Eu}/\text{Fe}]$ occurs, corresponding to the onset of the second source of Eu, namely NSMs, and then $[\text{Eu}/\text{Fe}]$ decreases again until super-solar metallicities. This bump in $[\text{Eu}/\text{Fe}]$ is not supported at all by the observations, indicating that if NSMs do contribute to the production of Eu in the thin disc then this contribution should be small enough to not compensate the decrease in $[\text{Eu}/\text{Fe}]$ due to the release of Fe by SNe Ia. Moreover, model D always under-predicts the Eu abundance for the outer disc and the solar ring; only the inner-disc curve matches the inner-disc OC data.

Figure 5 displays the field-star and OC samples, and models C and D in the $[\text{Eu}/\text{Fe}]$ versus age plane. We find OCs with enhanced $[\text{Eu}/\text{Fe}]$ (≥ 0.2) of any age between 1 and 7 Gy and they tend to be located in the outer part of the Galaxy. OCs with solar or sub-solar $[\text{Eu}/\text{Fe}]$ tend to be younger (less than 4 Gy old) and located in the solar-neighbourhood or inner Galaxy. This is in line with the model of inside-out formation of the Galactic disc (Bergemann et al. 2014). We remark that the agreement between model C and observations in this parameter plane is not as good as in the $[\text{Eu}/\text{Fe}]$ versus $[\text{Fe}/\text{H}]$ plane. The global trend is correct: $[\text{Eu}/\text{Fe}]$ increases with increasing age for each Galactocentric region, the solar-ring and outer Galaxy exhibit larger $[\text{Eu}/\text{Fe}]$ compared to the inner Galaxy at any age bin. However, the inner-disc and outer-disc curves underestimate the $[\text{Eu}/\text{Fe}]$ ratio compared to the inner-disc and outer-disc OC subsamples, respectively. The solar-ring curve yields the most satisfactory match with the observed data. Though this discrepancy was already noticed in Fig. 4, it is more visible in the $[\text{Eu}/\text{Fe}]$ versus age plane. Keeping in mind that the typical uncertainty on the age for the field-star sample is about 1.7 Gy (mean of age uncertainty from isochrone fitting), we find a flat $[\text{Eu}/\text{Fe}]$ versus age distribution for the field-star sample, indicating a mixing of the stellar population with a different chemical history. On the other hand, the disagreement between model D and the data is worse: the offset between the solar-ring and outer-disc curves and the observed OC data is larger than with model C at any age.

4.2. The evolution of Mg

Figures 6 and 7 show the observed $[\text{Mg}/\text{Fe}]$ as a function of $[\text{Fe}/\text{H}]$ and of stellar age, respectively, along with the three models tested for Mg production, namely models A, B, and C described in Sect. 3. We recall that the main change between the three models is how much SNe Ia contribute to the Mg production.

In Fig. 6, the field-star Mg-to-Fe ratio displays the well-known pattern for an α -element in the Milky Way: for thick-disc stars, a plateau at $[\text{Mg}/\text{Fe}] \sim 0.4$ up to a metallicity of -0.8 ; for both thin- and thick-disc stars, a decrease in $[\text{Mg}/\text{Fe}]$ with increasing metallicity, with a possible flattening around $[\text{Mg}/\text{Fe}] \sim 0$ for super-solar metallicities. The open-cluster Mg-to-Fe ratios also exhibit a decreasing trend with increasing metallicity, overlapping the thin-disc sequence. The best agreement between the observations and our models is reached for

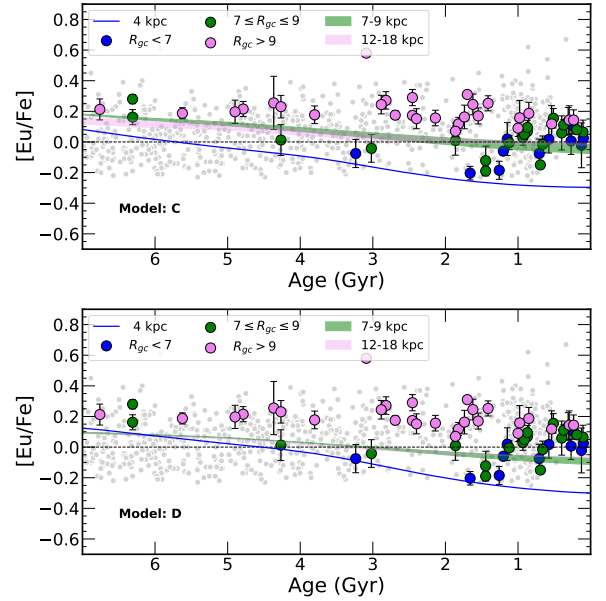


Fig. 5. $[\text{Eu}/\text{Fe}]$ vs. age for the field-star and open-cluster samples. Same symbols and colours as in Fig. 4.

model C, in which the production of Mg is due to both CCSNe and SNe Ia. In this model, the yields of SNe Ia are metallicity-dependent in order to reproduce the behaviour of younger, metal-rich clusters. This choice affects not only the super-solar region, where, as already noted in Magrini et al. (2017), the decline of $[\text{Mg}/\text{Fe}]$ is not observed, but also the sub-solar region, with a lower enhancement at low metallicities. The value of $[\text{Mg}/\text{Fe}]$ for thin-disc MW field stars in the super-solar metallicity regime is a debated topic, both by observers and theoreticians. It is well known from spectroscopists that abundance determination is not an easy task and that, despite their careful work, it is difficult to identify and correct any bias introduced during the spectral analysis (see, e.g., the discussion in Jofré et al. 2017). Santos-Peral et al. (2020) investigated the role of the continuum placement in the derived Mg abundances. After a thorough testing of the pseudo-normalisation procedure, they claim that $[\text{Mg}/\text{Fe}]$ continues to decrease for $[\text{Fe}/\text{H}] \geq 0$ instead of flattening. However, their conclusion is weakened by the fact that among their selected Mg lines, only the four saturated lines support this decrease, while the five weak lines show a flattening (their Fig. 16). On the other hand, Galactic chemical evolution models are not robust enough to determine the most likely solution: for instance, Matteucci et al. (2019) was able to reproduce the flattening of the Mg-to-Fe ratios observed in the APOGEE dataset (e.g., Jönsson et al. 2020) by increasing the contribution of SNe Ia to Mg production (similar to what is done in this work), but Matteucci et al. (2020) still wondered whether the flattening is an artefact or not.

Figure 7 shows the $[\text{Mg}/\text{Fe}]$ versus age plane. In this plane, we do not separate the sequences for the inner-disc, solar-neighbourhood, and outer-disc open clusters: for most OCs, $[\text{Mg}/\text{Fe}]$ appear compatible with a single linear function of age. The only exception is observed for a handful of inner-disc, young, α -enhanced open clusters (see next paragraph). The best agreement between the data and the models is obtained with model C. In model A, the curve for the inner-disc differs greatly from the data of inner-disc open clusters: at an age of ≈ 1 Gy, the inner-disc curve of model A predicts $[\text{Mg}/\text{Fe}] \approx -0.2$, compared to the observed ratio of ≈ 0 ; for the youngest open clusters, the

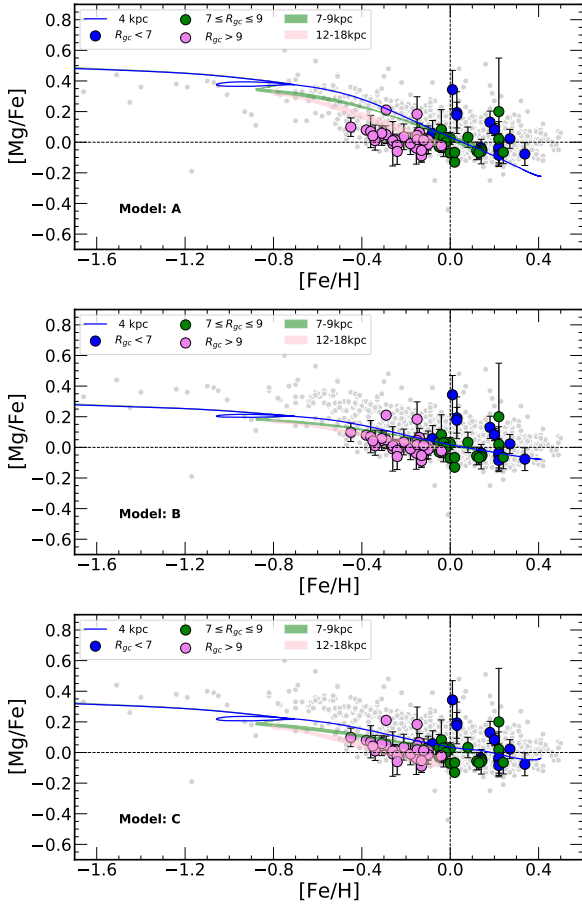


Fig. 6. $[\text{Mg}/\text{Fe}]$ vs. $[\text{Fe}/\text{H}]$ for the field-star sample and the OC sample. The symbols and colours are the same as in Fig. 4. Three models are considered: Model A (upper panel), model B (middle panel), and model C (bottom panel).

disagreement is even larger. We note that when the contribution of SNe Ia to Mg is increased (models B and C), the theoretical curves for the three Galactic regions considered here come closer to each other, which is compatible with our OC data.

As noted in earlier works (Magrini et al. 2014, 2017; Casamiquela et al. 2018), there is a population of inner clusters that are α -enhanced, which is also clearly visible in our data. Chiappini et al. (2015) was among the first papers to report the existence of a young α /Fe-enhanced population in the CoRoT (Miglio et al. 2013) and APOGEE (Majewski et al. 2017) samples. They discovered several young stars with unexpectedly high α /Fe abundances, located in the inner disc. A similar population is also present in other works (e.g., Haywood et al. 2013; Bensby et al. 2014; Bergemann et al. 2014; Martig et al. 2015). For field stars, several works have investigated the role of mass transfer and binarity to explain their chemical pattern (see, e.g., Jofré et al. 2016; Hekker & Johnson 2019; Sun et al. 2020; Zhang et al. 2021). However, while for field stars, there is still a possible ambiguity in the determination of their ages and masses, even when it is done with asteroseismology, such uncertainty disappears when it concerns the determination of the ages of stars in clusters. For the α -enhanced clusters, we need a different explanation, such as chemical evolution and migration. A possible interpretation is that the α -enhanced clusters might have been born in a region near the corotation of the bar where the gas can be kept inert for a long time and in which the enrichment is

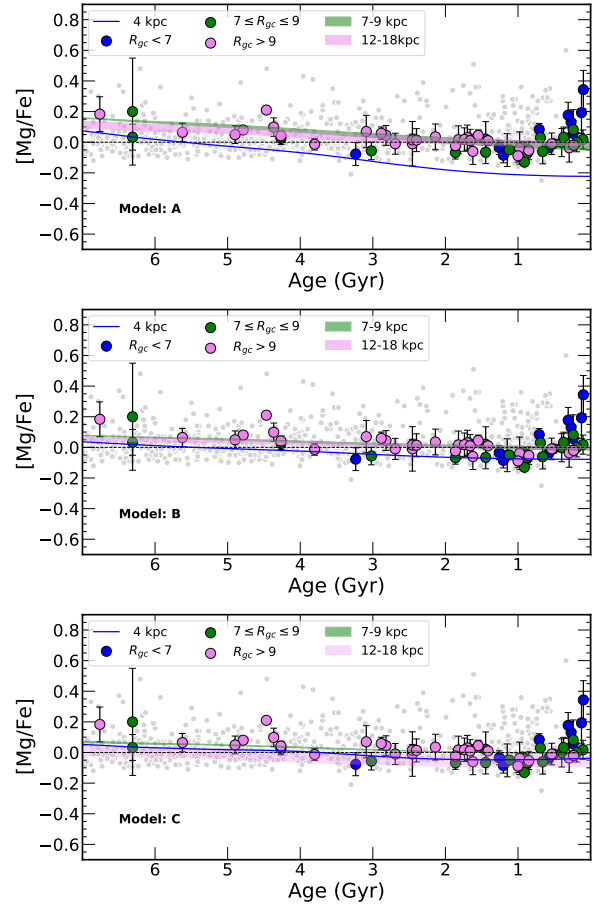


Fig. 7. $[\text{Mg}/\text{Fe}]$ vs. age for the field-star sample and the OC sample. The symbols and colours are the same as in Fig. 4. Three models are considered: Model A (upper panel), model B (middle panel), and model C (bottom panel).

due only to CCSNe (Chiappini et al. 2015). Further migration might have moved them to their current radius.

4.3. The evolution of O

We show the evolution of $[\text{O}/\text{Fe}]$ as a function of $[\text{Fe}/\text{H}]$ and of age in Figs. 8 and 9, respectively. For oxygen, we considered only its production by CCSNe, with short timescales, and therefore, we display only the set of curves for model C. We remind the reader that the forbidden $[\text{OI}]$ line may be affected by telluric lines, preventing a reliable abundance measurement under specific conditions; hence the reduced number of data points for this chemical species (e.g., Nissen & Edvardsson 1992, and in particular their Fig. 2 displaying such an OI line affected by the telluric blend). Field stars exhibit a decrease from $[\text{O}/\text{Fe}] \approx 0.4$ at $[\text{Fe}/\text{H}] \leq -0.7$ (upper limit because of the paucity of metal-poor stars with O determination) to $[\text{O}/\text{Fe}] \approx -0.3$ at $[\text{Fe}/\text{H}] \approx 0.4$. The open-cluster sample also exhibits a decrease in the O-to-Fe ratio with metallicity; the outer-disc OCs tend to be more O-enhanced than the inner-disc OCs. The three curves for model C corresponding to the inner disc, solar ring, and outer disc are compatible with our OC data, given the observational error bars. In the $[\text{O}/\text{Fe}]$ versus age plane, data and models are also in good agreement: $[\text{O}/\text{Fe}]$ decreases with decreasing age; at a given age, the outer-disc OCs tend to be more O-enhanced than the

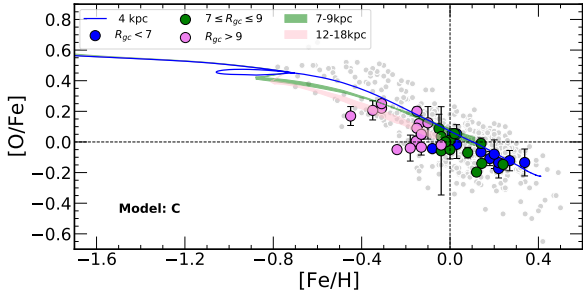


Fig. 8. $[O/Fe]$ vs. $[Fe/H]$ for the field-star sample and the OC sample. The symbols and colours are the same as in Fig. 4. Only model C is shown.

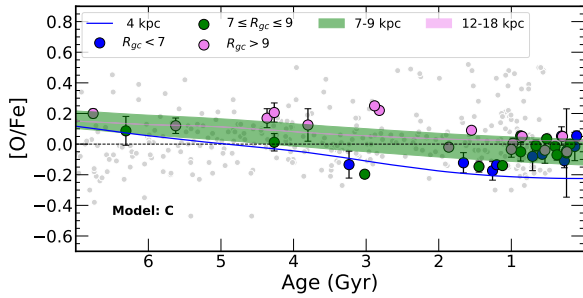


Fig. 9. $[O/Fe]$ vs. age for the field-star sample and the OC sample. The symbols and colours are the same as in Fig. 4. Only model C is shown.

inner-disc OCs; and young clusters (less than 2 Gy old), no matter their Galactocentric radius, have a solar or sub-solar $[O/Fe]$.

We note that the young, inner-disc, Mg-enhanced open clusters with solar or super-solar metallicity are not O-enhanced. Among the six OCs with $[Mg/Fe] \geq 0.05$, four have a metallicity very close to solar; in other words, a metallicity where the determination of Mg should not be concerned by the issues briefly discussed in the previous section. We cannot explain this difference through an analysis of systematic effects and we think this difference between Mg and O is genuine for this population of open clusters. Thus, this observational fact may be further evidence of the different nucleosynthetic paths needed to produce oxygen on the one hand and magnesium on the other hand, and it reminds us that the so-called α -elements are not interchangeable in the context of Galactic archaeology.

4.4. The evolution of $[Eu/Mg]$ and of $[Eu/O]$

The study and comparison of Eu with O and Mg is crucial in order to understand if this r -process element and those two α -elements share the same production sites or are released to the ISM over the same timescales. Such comparisons are particularly useful for probing the chemical enrichment of the early Galaxy. The interest in the $[Eu/Mg]$ ratio has also increased in recent years, due to its potential to unveil the extragalactic origin of some MW stars with unusual values (e.g., McWilliam et al. 2013; Lemasle et al. 2014; Xing et al. 2019; Skúladóttir et al. 2019; Matsuno et al. 2021). An increasing number of studies on $[Eu/Mg]$, based on increasingly larger samples of stars, are being published (see, e.g., Mashonkina & Gehren 2001; Mashonkina et al. 2003; Delgado Mena et al. 2017). More recently, Guiglion et al. (2018) addressed the subject for the AMBRE project using a large sample of about 1400 FGK Milky Way disc stars, reporting a decreasing r/α trend with increas-

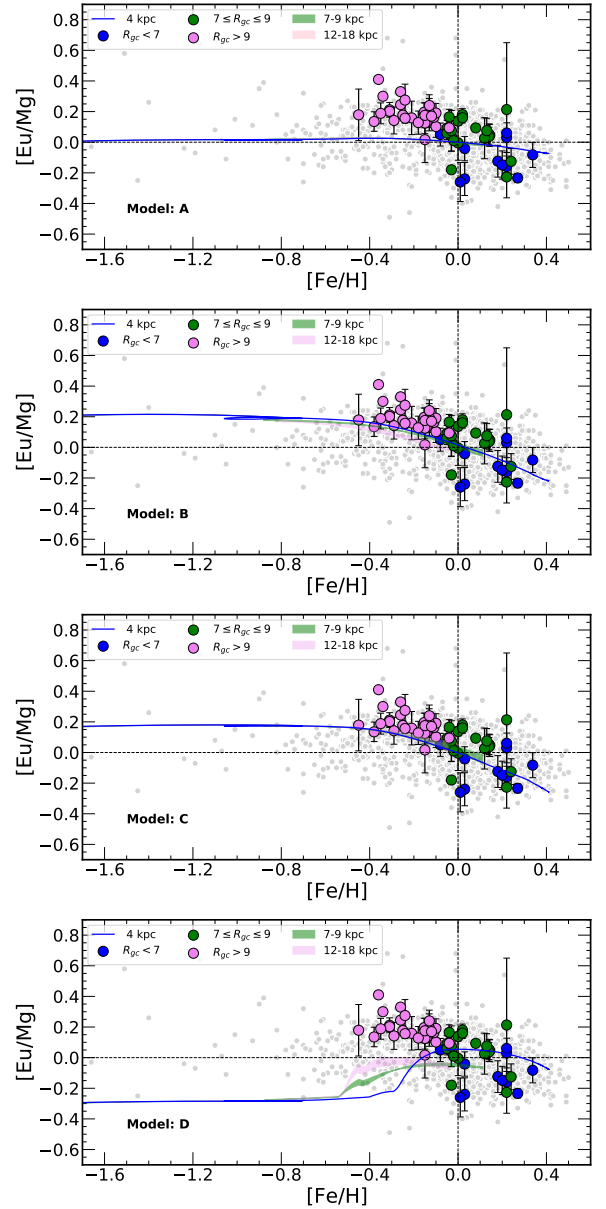


Fig. 10. $[Eu/Mg]$ vs. $[Fe/H]$ for the field-star sample and the OC sample. The symbols and colours are the same as in Fig. 4. Four models are considered. From top to bottom: Model A, model B, model C, and model D.

ing metallicity, and concluding that SNe involved in the production of Eu and Mg should have different properties. Tautvaišienė (2021) also found that the $[Eu/Mg]$ ratio decreases with metallicity for both thin- and thick-disc stars, the gradient being steeper for the thick disc.

Figure 10 shows the evolution of $[Eu/Mg]$ as a function of $[Fe/H]$ for the field-disc stars, the thin-disc OCs, and the four models A, B, C, and D. Our field-star sample displays a large scatter; however, $[Eu/Mg]$ tends to be around 0.2 at $[Fe/H] \sim -0.4$ and tends to be around -0.1 for $[Fe/H] \sim 0.3$. The linear regression yields a slope of -0.163 , a y -intercept of 0.015, and a Pearson correlation coefficient (PCC) of -0.30 . If we restrict our field stars to the solar region (7 to 9 kpc), our sample is reduced to 741 field stars with a slope of -0.162 (y -intercept = -0.002). These regression parameters are almost the same as those obtained using the sample of 506 stars from Tautvaišienė (2021):

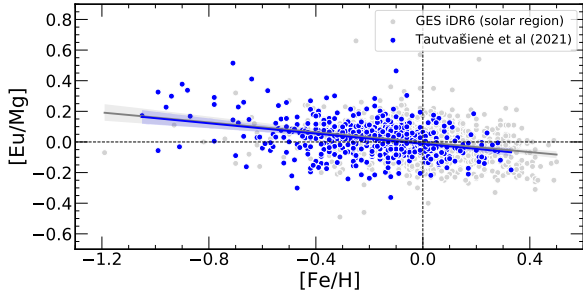


Fig. 11. [Eu/Mg] vs. [Fe/H] for our sample of field stars (grey dots) in the solar region, compared to those of Tautvaišienė (2021) in the solar neighbourhood (blue dots). The solid lines represent the linear regression lines, which seem to coincide for both samples, and the shaded regions show the confidence interval.

a slope of -0.167 and a y-intercept of -0.012 with a PCC of $= -0.33$ (see Fig. 11). On the other hand, our OC sample exhibits a steeper decreasing trend with a slope of -0.535 and a y-intercept of 0.055 with a PCC of $= -0.69$. The slope of the linear regression for field stars and OCs are not directly comparable because the OC sample encompasses a much larger region of the disc.

Model A, with a pure CCSNe production of Mg, results in a nearly constant [Eu/Mg] as a function of metallicity for the three Galactocentric regions. Model D, with a mixed production of Eu by MRD SNe and NSMs, and a pure CCSNe production of Mg, under-predicts the Eu-to-Mg ratios in almost any metallicity bin. Only models B and C, with a pure MRD SNe production of Eu and a mixed production of Mg by CCSNe and SNe Ia, yield a satisfactory match to the OC data. Model C gives slightly better results: it minimises the under-prediction of the Eu-to-Mg ratio for the outer-disc OCs, it predicts slightly lower Eu-to-Mg ratios at $[\text{Fe}/\text{H}] \sim 0.3$ than model B. Given that model C was also the best-matching model in the [Eu/Fe] versus [Fe/H] plane and the [Mg/Fe] versus [Fe/H] plane (see Sects. 4.1 and 4.2), we conclude from Fig. 10 that a) the production of Eu in the thin disc can be explained solely by a production by MRD SNe and b) the production of Mg should involve at least two sources, namely CCSNe and SNe Ia with metal-dependent yields.

Trevisan & Barbuy (2014) studied the [Eu/O] ratio versus metallicity, age, and Galactocentric distance in a sample of 70 old and metal-rich, thin- and thick-disc dwarf stars selected from the NLTT catalogue. Combined with the literature data, they found a steady increase in Eu-to-O with metallicity over the metallicity range $[-1, 0.5]$. On the other hand, Haynes & Kobayashi (2019) provided galactic simulations of *r*-process elemental abundances, comparing them with observations from the HERMES-GALAH survey. These observations show a flat [Eu/O] trend as a function of [Fe/H], suggesting that europium is produced primarily at the same rate as oxygen.

Figure 12 shows the evolution of [Eu/O] as a function of [Fe/H] for the field-disc stars, the thin-disc OCs, and models C and D. Once again, the best-matching model is model C. The curves corresponding to the three Galactocentric regions under study are indiscernible and are about 0.15 lower than the OC data over the metallicity range $[-0.4, 0.4]$. This under-prediction of the Eu-to-O ratio in the models results from the slight under-prediction of the Eu-to-Fe ratio seen in Fig. 4 and the over-prediction of O-to-Fe ratio seen in Fig. 8. On the other hand, the Eu-to-O ratio for the OC sample exhibits a flat trend and only model C is able to reproduce this feature. Model D, assuming a production of Eu by both MRD SNe and NSMs, seems to

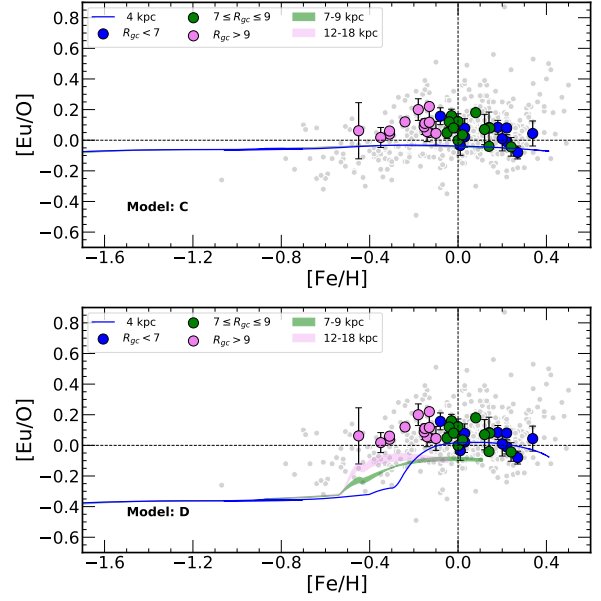


Fig. 12. [Eu/O] vs. [Fe/H] for the field-star sample and the OC sample. The symbols and colours are the same as in Fig. 4. Two models are considered: Model C (upper panel) and model D (bottom panel).

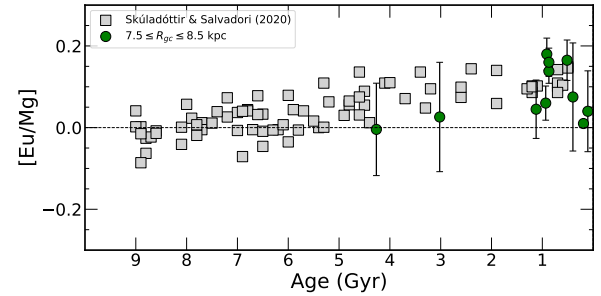


Fig. 13. [Eu/Mg] vs. age (Gy) for our sample of open clusters in an R_{gc} range of 7.5–8.5 kpc (green circles) compared with the solar twins (grey squares) from Skúladóttir & Salvadori (2020), with data from Spina et al. (2018; ages, Eu abundances) and Bedell et al. (2018; Mg abundances).

under-predict the Eu-to-O ratio by 0.2 at $[\text{Fe}/\text{H}] \sim -0.6$ when compared to field stars. After a rapid increase in [Eu/O] due to the onset of NSMs, model D predicts a flattening of the Eu-to-O ratio for the three Galactocentric regions. However, only the inner-disc curve matches the corresponding OC data. Thus, the Eu-to-O ratio diagnostic also speaks in favour of a common origin of Eu and O in the thin disc, and therefore favours a rapid production of Eu by MRD SNe.

Finally, in Fig. 13, we show [Eu/Mg] with respect to age for the solar-twins sample discussed in Skúladóttir & Salvadori (2020; sample based on Spina et al. 2018; Bedell et al. 2018) and for our OC sample, restricted to the solar neighbourhood. More specifically, we selected only the OCs in a radial region close to that of the solar twins ($R_{\text{GC}} \sim 7.5\text{--}8.5$ kpc) and we excluded the clusters likely affected by migration (NGC 6971, Berkeley 44, and Collinder 261; see VV22 for more details on clusters' orbits and migration). The data of the solar twins and of the open clusters agree in the age range in which they overlap. Skúladóttir & Salvadori (2020) claim to detect a change in the slope in the [Eu/Mg] versus age plane occurring 4 Gy ago, signalling the rise of Eu production by NSMs. Given the short

Table 3. Model significance for the solar-twins sample: assumed regressions and F -value.

H_0	$[\text{Eu}/\text{Mg}] = 0.0168 \times \text{age} + 0.1328$
H_1	$[\text{Eu}/\text{Mg}] = 0.0076 \times \text{age} + 0.1181$ for $\text{age} \leq 4$ Gyr $[\text{Eu}/\text{Mg}] = 0.0175 \times \text{age} + 0.1367$ for $\text{age} > 4$ Gyr
F -value	0.4643
F -critical	3.119

Notes. The critical F -value is given for a right-tailed test, with a false-rejection probability $\alpha = 0.05$, and the two degrees of freedom are 2 and 75.

age interval spanned by the solar-ring OCs (younger than 6 Gy), they cannot be used to investigate this change in slope. However, we would like to stress that the flattening modelled by Skúladóttir & Salvadori (2020) does not appear to be statistically significant. Indeed if we perform an F-test, choosing for the null hypothesis H_0 ‘the solar-twins distribution is described by a single linear-regression’ and the alternative hypothesis H_1 ‘the solar-twins distribution is described by two piece-wise linear-regressions’, then we cannot reject H_0 at the 95 % level (see Table 3).

Figures 14 and 15 display the radial gradient for $[\text{Eu}/\text{Mg}]$ and $[\text{Eu}/\text{O}]$, respectively. We note an increasing trend in $[\text{Eu}/\text{Mg}]$ with Galactocentric radius from the OC sample. This can be explained by the fact that Mg and Eu are produced via different nucleosynthetic channels: a non-negligible production of Mg by a delayed mechanism (e.g., SNe Ia) in the context of inside-out formation of the Galactic disc would explain why $[\text{Eu}/\text{Mg}]$ becomes negative first at smaller radii. On the other hand, $[\text{Eu}/\text{O}]$ is flat over the probed Galactic radii. This is compatible with a scenario where O and Eu are produced by the same progenitors, namely CCSNe.

4.5. Other r -process elements

The distributions of heavy elements synthesised by the s -process are characterised by the presence of three peaks, corresponding to neutron magic numbers 50, 82, and 126. The s -process-dominated elements belonging to the first peak are Sr, Y, and Zr. Those belonging to the second peak are Ba, La, and Ce. Close to these peaks, there are elements (such as Mo, Nd, and Pr), whose origins are shared between the s -process and the r -process. As a matter of fact, the contributions from the two nucleosynthesis processes (and eventually from the p -process) are almost equal, at least in the age and metallicity range of the disc.

Estimates of the contributions of the different processes to their abundances in the Sun vary from one author to another (e.g., Arlandini et al. 1999; Simmerer et al. 2004; Sneden et al. 2008; Bisterzo et al. 2014; Prantzos et al. 2020), but they all agree on assigning them a non-negligible percentage of r -process, in some cases more than 50%. Indeed, the s -process-dominated elements seem to be placed in the second to fourth IUPAC groups of the periodic table (Sr, Ba, Y, La, Zr, Ce); the mixed elements in the fifth to sixth groups (Pr, Mo, Nd), and the r -process-dominated elements in the eighth and ninth (Ru, Sm, and Eu). This suggests, in most of the cases, an increase in the r -process component from left to right in the periodic table, group by group, for the aforementioned elements, or, equivalently, by increasing its ionisation energy. In the following paragraph, we concentrate on the mixed elements Mo, Nd, and Pr.

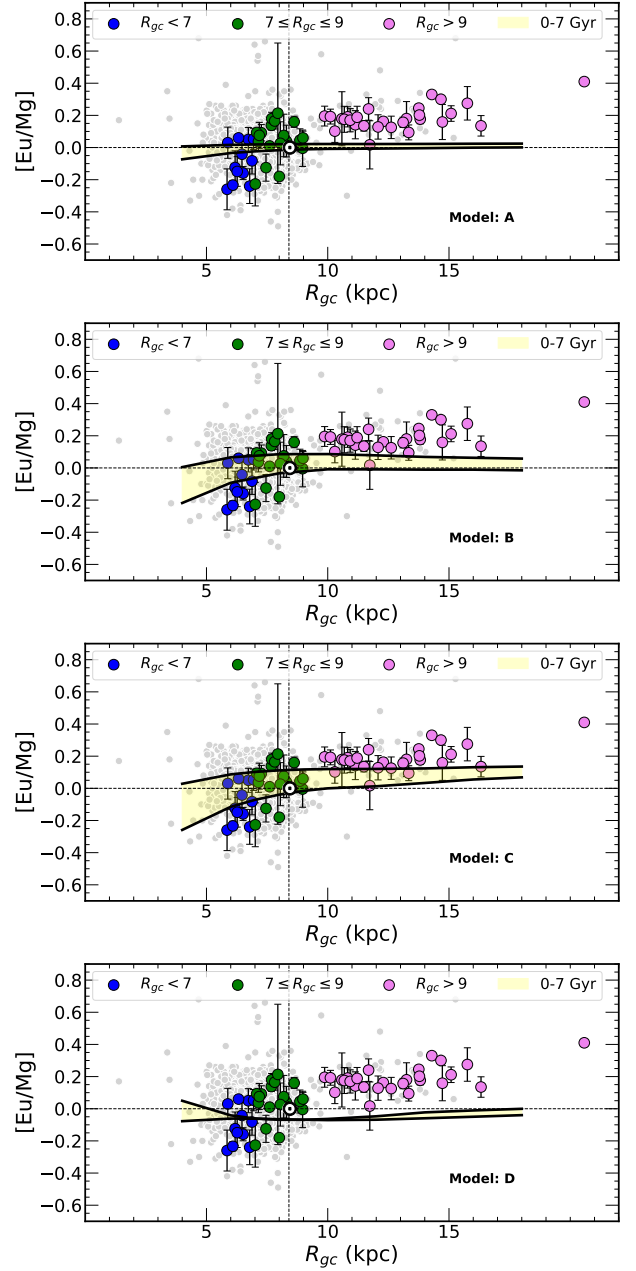


Fig. 14. $[\text{Eu}/\text{Mg}]$ vs. R_{GC} for the field-star sample and the OC sample. The symbols and colours are the same as in Fig. 4. Four models are considered. From top to bottom: Model A, model B, model C, and model D.

For the elements in the present work, by considering everything that does not originate from the s -process as produced by the r -process, the above-quoted works agree in assigning $\sim 40\%$ of the r -process component to Nd and $\sim 50\%$ to Pr. For Mo, there is less consensus. Bisterzo et al. (2014) attribute more than 60% of its origin to the r -process component, while Cowan et al. (2021) attribute to Mo an almost complete origin from the r -process. On the other hand, Prantzos et al. (2020) proposed a percentage of 50% to the s -process and 27% to the r -process, assigning the remaining 23% to the p -process (in which photo-disintegrations produce proton-rich nuclei starting from pre-existing heavy isotopes; see, e.g., Mishenina et al. 2019).

We examine the origin of these elements from an observational point of view, comparing their abundance with that

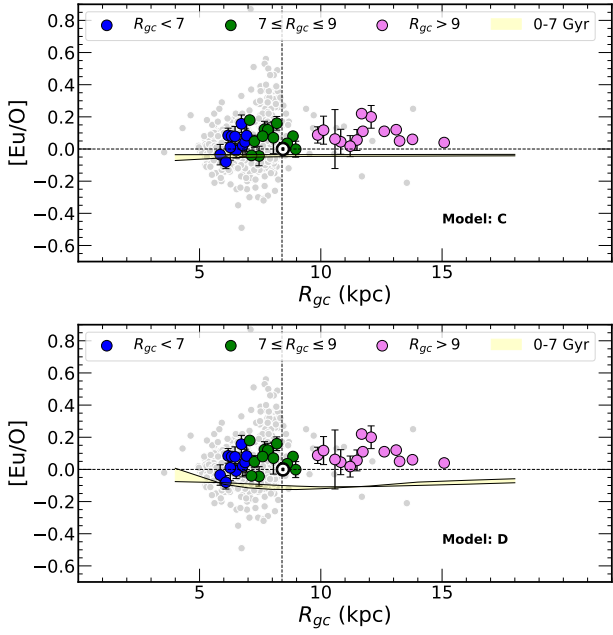


Fig. 15. [Eu/O] vs. R_{GC} for the field-star sample and the OC sample. The symbols and colours are the same as in Fig. 4. Two models are considered: Model C (upper panel) and model D (bottom panel).

of Eu. In Fig. 16, we present [El/Eu] versus [Fe/H] for Mo, Pr, and Nd both in clusters and field stars. In the figure, for each element we also show the r -process percentage in the Sun proposed by Prantzos et al. (2020). For molybdenum, we also report an intermediate level, determined by the sum of the r -component and the p -component. If the elements were produced only by the r -process at all metallicities, we would expect to find their abundances close to the lines that indicate the sole r -process contribution. To reach the observed abundances at the typical metallicity of the disc, a contribution from the s -process is required. The metallicity at which [El/Fe] starts to increase is different for Mo, Pr, and Nd, indicating different timescales for their production.

Neodymium. Among the three elements, Nd has the flattest trend, and thus we cannot identify the metallicity corresponding to the transition between the r -process-dominated regime and the s -process-dominated regime, since the contribution of the s -process might start at lower metallicities, at least as far as clusters are concerned. Its flat profile with respect to europium and the difference of about 0.4 with respect to its r -process abundance points to a significant s -process contribution of the same order of the r -process contribution over the disc metallicity range.

Praseodymium. The same does not hold for Praseodymium, for which a lower s -process contribution is expected. As a matter of fact, an increasing trend in [Pr/Eu] with increasing [Fe/H] is well defined, indicating a recent enrichment by the s -process (starting from about [Fe/H] ~ -0.4 , as an upper limit). However, the r -process component still dominates the Pr production at a high metallicity, as recently reported by Tautvaišienė (2021) for about 500 thin- and thick-disc stars in the solar neighbourhood.

Molybdenum. Finally, Mo abundances show quite a flat trend, characterised by a greater scatter than for Pr and Nd. We also note that this scatter tends to increase with decreasing metallicity. The contribution from the s -process seems to

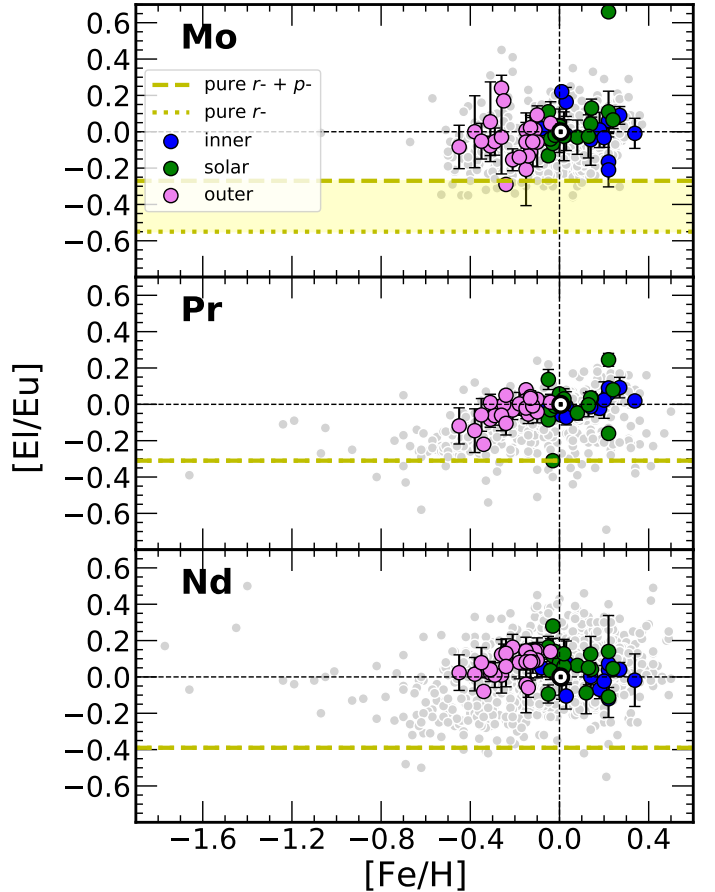


Fig. 16. [El/Eu] vs. [Fe/H] for the mixed elements: Mo, Pr, and Nd. Data for both the field-star sample and OC sample are shown. The symbols and colours are the same as in Fig. 4. The dashed yellow lines track the pure contribution of the r -process derived using the solar abundances from Grevesse et al. (2007), and the most recent percentages from Prantzos et al. (2020) for the r -process and the $r + p$ -process for Mo.

have started at lower metallicities than those we sampled with the OCs. This behaviour was also observed by Mishenina et al. (2019). Such a scatter is closely related to the elusive nature of this chemical element and to the difficulty in measuring its abundance. As a matter of fact, different GCE studies have reached discordant conclusions on this element, proposing various solutions to reach a better agreement between theory and observations. Mishenina et al. (2019) concluded that canonical stellar sources of heavy elements do not produce enough Mo, while Kobayashi et al. (2020) stated that the disagreement can be mitigated by including the ν -wind from nascent neutron stars. Finally, Prantzos et al. (2020) ascribed to the p -process the missing percentage to reproduce the Solar composition. On top of that, recent spectroscopic observations of heavy elements in barium stars (which are thought to have been polluted by the s -process at work in the already extinct AGB companion) highlighted that the enhancements of Nb, Mo, and Ru are larger than those expected by current available s -process models (Roriz et al. 2021). For these elements, Ba stars show enrichment that is definitely larger than enrichment found in field stars, pointing to a process at work in those binary systems (thus excluding a different pristine chemical distribution, more easily attributable to the r -process). This would be at odds with the conclusions by Mishenina et al. (2019), who excluded the s -process as responsible for such a peculiar chemical feature.

Further studies on this topic are urgently needed, possibly focusing on the improvement of the nuclear inputs adopted to run nucleosynthesis models.

5. Summary and conclusions

With the aim of shedding light on the most prominent sources for the *r*-process in the Galactic disc, we compared the abundance of Eu, which is an element mainly produced by the *r*-process, with those of the two α -elements (Mg and O), expected to be mostly originated in core-collapse SNe on short timescales. For this purpose, we relied on a large sample of open clusters from the recently released *Gaia*-ESO iDR6, which gave us the advantage of containing one of the largest and most complete samples of open clusters, distributed in age and Galactocentric distance, in which abundances of neutron capture elements have been measured. We complemented our sample of open clusters with a sample of field stars. As it is known, our ability to obtain ages for field stars is limited, but they can still complement the information we get from clusters, as they have an age distribution that reaches older ages.

We built up a GCE model, in which we made several choices for Eu and Mg nucleosynthesis (models A to D). For Eu, we considered two possible mechanisms of production: a fast production in CCSNe (e.g., magneto-rotationally driven SNe) and a combination of CCSNe and delayed production in NSMs with a delay of 3 Gy. For Mg, we considered three different cases: CCSNe, CCSNe and SNe Ia, and finally CCSNe and SNe Ia with metallicity-dependent yields. We compared the observations with the results of the model(s) in different planes ([Eu/Fe] vs. age, [Eu/Fe] vs. [Fe/H], and [Eu1/Eu2] vs. age and [Fe/H]). The first conclusion of the model-observation comparison is that for Eu, at the metallicity of the disc, it is not necessary to introduce a delayed component (e.g., from NSMs). The fast production is sufficient to reproduce the observational data. In order to make a meaningful comparison of Eu abundance with the abundance of O and Mg, we have studied their chemical evolution: for oxygen, a rapid source (CCSNe) is sufficient to explain the observations, while for Mg, a growth (flattening in the [Mg/Fe] vs. [Fe/H] plane) is clearly visible in the data, which we have explained as the contribution of SNe Ia at a high metallicity. Although not directly related to the main purpose of our work, the differences between O and Mg show that α -elements are not interchangeable with each other, and that great care must be taken in their correct use. In particular, Mg has a larger production from SNe Ia at a high metallicity than usually expected, and it cannot be considered a ‘pure’ α -element, at least in the metallicity range of the Galactic disc.

Once the origin of Mg and O has been established, comparison with Eu gives us a further key to understanding the origin of this element. On the one hand, the observations show a growth of [Eu/Mg] at a low metallicity, which can be correctly explained by the model only if we consider that Eu and Mg have a different origin. In particular, Eu does not share the same delayed production as Mg at a high metallicity (see model C). On the other hand, within the uncertainties, [Eu/O] has a flat trend with metallicity, pointing towards a common origin (or, better, towards common timescales) for these two elements. The model with a delayed production of Eu clearly underestimates the [Eu/O] ratio at a low metallicity. Finally, the observations of star clusters show a positive radial gradient of [Eu/Mg] in the disc, which again can be explained by the combination of the inside-out growth of the disc and the delayed extra-production of Mg at a high metallicity (not yet reached in the outer disc). The radial gradient of [Eu/O]

is, on the other hand, almost flat (a small offset between the data and the model is present), indicating again similar timescales for their production.

We can therefore conclude that the europium we observe in field and cluster populations at the thin-disc metallicities is predominantly produced by sources with short lifetimes, such as magneto-rotationally driven SNe or collapsars. The same role can be played by NSMs if their mergers take place with a very short delay (Matteucci 2014) or – in the context of a time delay distribution – if their frequency was higher at a low metallicity (Simonetti et al. 2019; Cavallo et al. 2021). Indeed, with these assumptions, their enrichment can mimic the fast pollution by CCSNe. Introducing the NSMs as an additional source can still be an option, but according to our results, it appears to be negligible at thin-disc metallicities (cf. Skúladóttir & Salvadori 2020).

Finally, we analysed three mixed elements (Mo, Pr, and Nd) to which a non-negligible origin in the *r*-process is attributed. For each of them, we discuss the component produced by the *r*-process. The most interesting case is represented by molybdenum, whose cosmic origin is still a debated matter and deserves dedicated studies in the future.

Acknowledgements. We thank the anonymous referee for their relevant questions and remarks that helped us in improving the presentation and the discussion of the results. Based on data products from observations made with ESO Telescopes at the La Silla Paranal Observatory under programme ID 188.B-3002, 193.B-0936, 197.B-1074. These data products have been processed by the Cambridge Astronomy Survey Unit (CASU) at the Institute of Astronomy, University of Cambridge, and by the FLAMES/UVES reduction team at INAF/Osservatorio Astrofisico di Arcetri. These data have been obtained from the *Gaia*-ESO Survey Data Archive, prepared and hosted by the Wide Field Astronomy Unit, Institute for Astronomy, University of Edinburgh, which is funded by the UK Science and Technology Facilities Council. This work was partly supported by the European Union FP7 programme through ERC grant number 320360 and by the Leverhulme Trust through grant RPG-2012-541. We acknowledge the support from INAF and Ministero dell’ Istruzione, dell’ Università’ e della Ricerca (MIUR) in the form of the grant “Premiale VLT 2012” and “Premiale 2016 MITIC”. The results presented here benefit from discussions held during the *Gaia*-ESO workshops and conferences supported by the ESF (European Science Foundation) through the GREAT Research Network Programme. TB was funded by grant No. 621-2009-3911 and grant No. 2018-0485 from The Swedish Research Council. FJE acknowledges financial support by the Spanish grant MDM-2017-0737 at Centro de Astrobiología (CSIC-INTA), Unidad de Excelencia María de Maeztu. TM acknowledges financial support from the Spanish Ministry of Science and Innovation (MICINN) through the Spanish State Research Agency, under the Severo Ochoa Program 2020-2023 (CEX2019-000920-S). LS is supported by the Italian Space Agency (ASI) through contract 2018-24-HH.0 to the National Institute for Astrophysics (INAF). This work has made use of data from the European Space Agency (ESA) mission *Gaia* (<https://www.cosmos.esa.int/gaia>), processed by the *Gaia* Data Processing and Analysis Consortium (DPAC, <https://www.cosmos.esa.int/web/gaia/dpac/consortium>). Funding for the DPAC has been provided by national institutions, in particular the institutions participating in the *Gaia* Multilateral Agreement. CVV and LM thank the COST Action CA18104: MW-Gaia. GC and AK acknowledge ChETEC-INFRA (EU project no. 101008324). DV acknowledges financial support from the German-Israeli Foundation (GIF No. I-1500-303.7/2019). MB is supported through the Lise Meitner grant from the Max Planck Society. We acknowledge support by the Collaborative Research centre SFB 881 (projects A5, A10), Heidelberg University, of the Deutsche Forschungsgemeinschaft (DFG, German Research Foundation). This project has received funding from the European Research Council (ERC) under the European Union’s Horizon 2020 research and innovation programme (Grant agreement No. 949173)

References

- Abbott, B. P., Abbott, R., Abbott, T. D., et al. 2017, *ApJ*, **848**, L12
- Arlandini, C., Käppeler, F., Wisshak, K., et al. 1999, *ApJ*, **525**, 886
- Baratella, M., D’Orazi, V., Carraro, G., et al. 2020, *A&A*, **634**, A34
- Baratella, M., D’Orazi, V., Sheminova, V., et al. 2021, *A&A*, **653**, A67
- Bedell, M., Bean, J. L., Meléndez, J., et al. 2018, *ApJ*, **865**, 68
- Bensby, T., Feltzing, S., & Lundström, I. 2004, *A&A*, **415**, 155

- Bensby, T., Feltzing, S., & Oey, M. S. 2014, *A&A*, 562, A71
- Bergemann, M., Ruchti, G. R., Serenelli, A., et al. 2014, *A&A*, 565, A89
- Bisterzo, S., Travaglio, C., Gallino, R., Wiescher, M., & Käppeler, F. 2014, *ApJ*, 787, 10
- Bramante, J., & Linden, T. 2016, *ApJ*, 826, 57
- Brauer, K., Ji, A. P., Drout, M. R., & Frebel, A. 2021, *ApJ*, 915, 81
- Buder, S., Sharma, S., Kos, J., et al. 2021, *MNRAS*, 506, 150
- Burbidge, E. M., Burbidge, G. R., Fowler, W. A., & Hoyle, F. 1957, *Rev. Mod. Phys.*, 29, 547
- Cantat-Gaudin, T., Anders, F., Castro-Ginard, A., et al. 2020, *A&A*, 640, A1
- Casamiuela, L., Carrera, R., Balaguer-Núñez, L., et al. 2018, *A&A*, 610, A66
- Cavallo, L., Cescutti, G., & Matteucci, F. 2021, *MNRAS*, 503, 1
- Cescutti, G., & Chiappini, C. 2014, *A&A*, 565, A51
- Cescutti, G., Matteucci, F., François, P., & Chiappini, C. 2007, *A&A*, 462, 943
- Cescutti, G., Romano, D., Matteucci, F., Chiappini, C., & Hirschi, R. 2015, *A&A*, 577, A139
- Chiappini, C. 2005, *Am. Inst. Phys. Conf. Ser.*, 804, 257
- Chiappini, C., Matteucci, F., & Gratton, R. 1997, *ApJ*, 477, 765
- Chiappini, C., Matteucci, F., & Romano, D. 2001, *ApJ*, 554, 1044
- Chiappini, C., Anders, F., Rodrigues, T. S., et al. 2015, *A&A*, 576, L12
- Côté, B., Eichler, M., Arcones, A., et al. 2019, *ApJ*, 875, 106
- Cowan, J. J., Sneden, C., Lawler, J. E., et al. 2021, *Rev. Mod. Phys.*, 93, 015002
- Cristallo, S., Piersanti, L., Straniero, O., et al. 2011, *ApJS*, 197, 17
- Cristallo, S., Straniero, O., Piersanti, L., & Gobrecht, D. 2015, *ApJS*, 219, 40
- Delgado Mena, E., Tsantaki, M., Adibekyan, V. Z., et al. 2017, *A&A*, 606, A94
- Denissenkov, P. A., Herwig, F., Woodward, P., et al. 2019, *MNRAS*, 488, 4258
- Famiano, M. A., Boyd, R. N., Kajino, T., et al. 2008, *J. Phys. G Nucl. Phys.*, 35, 025203
- François, P., Matteucci, F., Cayrel, R., et al. 2004, *A&A*, 421, 613
- Frebel, A. 2018, *Ann. Rev. Nucl. Part. Sci.*, 68, 237
- Fujimoto, S.-I., Kotake, K., Yamada, S., Hashimoto, M.-A., & Sato, K. 2006, *ApJ*, 644, 1040
- Gallino, R., Arlandini, C., Busso, M., et al. 1998, *ApJ*, 497, 388
- Gilmore, G., Randich, S., Asplund, M., et al. 2012, *The Messenger*, 147, 25
- Goriely, S., Bauswein, A., & Janka, H.-T. 2011, *ApJ*, 738, L32
- Goswami, P. P., Rathour, R. S., & Goswami, A. 2021, *A&A*, 649, A49
- Grevesse, N., Asplund, M., & Sauval, A. J. 2007, *Space Sci. Rev.*, 130, 105
- Guiglion, G., de Laverny, P., Recio-Blanco, A., & Prantzos, N. 2018, *A&A*, 619, A143
- Hampel, M., Stancliffe, R. J., Lugaro, M., & Meyer, B. S. 2016, *ApJ*, 831, 171
- Haynes, C. J., & Kobayashi, C. 2019, *MNRAS*, 483, 5123
- Haywood, M., Di Matteo, P., Lehnert, M. D., Katz, D., & Gómez, A. 2013, *A&A*, 560, A109
- Hekker, S., & Johnson, J. A. 2019, *MNRAS*, 487, 4343
- Hillebrandt, W., Nomoto, K., & Wolff, R. G. 1984, *A&A*, 133, 175
- Horowitz, C. J., Arcones, A., Côté, B., et al. 2019, *J. Phys. G Nucl. Phys.*, 46, 083001
- Jofré, P., Jorissen, A., Van Eck, S., et al. 2016, *A&A*, 595, A60
- Jofré, P., Heiter, U., Worley, C. C., et al. 2017, *A&A*, 601, A38
- Johansson, S., Litzén, U., Lundberg, H., & Zhang, Z. 2003, *ApJ*, 584, L107
- Jönsson, H., Holtzman, J. A., Allende Prieto, C., et al. 2020, *AJ*, 160, 120
- Jorissen, A., Boffin, H. M. J., Karinkuzhi, D., et al. 2019, *A&A*, 626, A127
- Kajino, T., Aoki, W., Balantekin, A. B., et al. 2019, *Prog. Part. Nucl. Phys.*, 107, 109
- Karakas, A. I., & Lugaro, M. 2016, *ApJ*, 825, 26
- Kasen, D., Metzger, B., Barnes, J., Quataert, E., & Ramirez-Ruiz, E. 2017, *Nature*, 551, 80
- Kobayashi, C., Karakas, A. I., & Lugaro, M. 2020, *ApJ*, 900, 179
- Korobkin, O., Rosswog, S., Arcones, A., & Winteler, C. 2012, *MNRAS*, 426, 1940
- Lattimer, J. M., & Schramm, D. N. 1974, *ApJ*, 192, L145
- Lemasle, B., de Boer, T. J. L., Hill, V., et al. 2014, *A&A*, 572, A88
- Liu, F., Asplund, M., Yong, D., et al. 2016, *MNRAS*, 463, 696
- Maeder, A., & Meynet, G. 2005, *A&A*, 440, 1041
- Magrini, L., Randich, S., Romano, D., et al. 2014, *A&A*, 563, A44
- Magrini, L., Randich, S., Kordopatis, G., et al. 2017, *A&A*, 603, A2
- Magrini, L., Spina, L., Randich, S., et al. 2018, *A&A*, 617, A106
- Majewski, S. R., Schiavon, R. P., Frinchaboy, P. M., et al. 2017, *AJ*, 154, 94
- Martig, M., Rix, H.-W., Silva Aguirre, V., et al. 2015, *MNRAS*, 451, 2230
- Mashonkina, L., & Gehren, T. 2001, *A&A*, 376, 232
- Mashonkina, L., Gehren, T., Travaglio, C., & Borkova, T. 2003, *A&A*, 397, 275
- Masseron, T., Johnson, J. A., Plez, B., et al. 2010, *A&A*, 509, A93
- Matsuno, T., Hirai, Y., Tarumi, Y., et al. 2021, *A&A*, 650, A110
- Matteucci, F. 2014, *The Origin of the Galaxy and Local Group*, Saas-Fee Advanced Course (Springer-Verlag, Berlin Heidelberg), 37, 145
- Matteucci, F., Grisoni, V., Spitoni, E., et al. 2019, *MNRAS*, 487, 5363
- Matteucci, F., Vasini, A., Grisoni, V., & Schultheis, M. 2020, *MNRAS*, 494, 5534
- McWilliam, A., Wallerstein, G., & Mottini, M. 2013, *ApJ*, 778, 149
- Miglio, A., Chiappini, C., Morel, T., et al. 2013, *MNRAS*, 429, 423
- Mishenina, T., Pignatari, M., Carraro, G., et al. 2015, *MNRAS*, 446, 3651
- Mishenina, T., Pignatari, M., Gorbaneva, T., et al. 2019, *MNRAS*, 489, 1697
- Naiman, J. P., Pillepich, A., Springel, V., et al. 2018, *MNRAS*, 477, 1206
- Nishimura, S., Kotake, K., Hashimoto, M.-A., et al. 2006, *ApJ*, 642, 410
- Nishimura, N., Takiwaki, T., & Thielemann, F.-K. 2015, *ApJ*, 810, 109
- Nissen, P. E., & Edvardsson, B. 1992, *A&A*, 261, 255
- Nomoto, K., Iwamoto, K., Nakasato, N., et al. 1997, *Nucl. Phys. A*, 621, 467
- Ojima, T., Ishimaru, Y., Wanajo, S., Prantzos, N., & François, P. 2018, *ApJ*, 865, 87
- Önehag, A., Korn, A., Gustafsson, B., Stempels, E., & Vandenberg, D. A. 2011, *A&A*, 528, A85
- Pancino, E., Lardo, C., Altavilla, G., et al. 2017, *A&A*, 598, A5
- Perego, A., Vescovi, D., Fiore, A., et al. 2022, *ApJ*, 925, 22
- Pian, E., D'Avanzo, P., Benetti, S., et al. 2017, *Nature*, 551, 67
- Prantzos, N., Abia, C., Cristallo, S., Limongi, M., & Chieffi, A. 2020, *MNRAS*, 491, 1832
- Ramírez, I., Meléndez, J., & Asplund, M. 2014, *A&A*, 561, A7
- Randich, S., Gilmore, G., & Gaia-ESO Consortium 2013, *The Messenger*, 154, 47
- Randich, S., Gilmore, G., Magrini, L., et al. 2022, *A&A*, 666, A121
- Romano, D., Karakas, A. I., Tosi, M., & Matteucci, F. 2010, *A&A*, 522, A32
- Roriz, M. P., Lugaro, M., Pereira, C. B., et al. 2021, *MNRAS*, 507, 1956
- Rosswog, S. 2005, *ApJ*, 634, 1202
- Sacco, G. G., Morbidelli, L., Franciosini, E., et al. 2014, *A&A*, 565, A113
- Santos-Peral, P., Recio-Blanco, A., de Laverny, P., Fernández-Alvar, E., & Ordenovic, C. 2020, *A&A*, 639, A140
- Simmerer, J., Sneden, C., Cowan, J. J., et al. 2004, *ApJ*, 617, 1091
- Simonetti, P., Matteucci, F., Greggio, L., & Cescutti, G. 2019, *MNRAS*, 486, 2896
- Skúladóttir, Á., & Salvadori, S. 2020, *A&A*, 634, L2
- Skúladóttir, Á., Hansen, C. J., Salvadori, S., & Choplin, A. 2019, *A&A*, 631, A171
- Smartt, S. J., Chen, T. W., Jerkstrand, A., et al. 2017, *Nature*, 551, 75
- Smiljanic, R., Korn, A. J., Bergemann, M., et al. 2014, *A&A*, 570, A122
- Sneden, C., Cowan, J. J., & Gallino, R. 2008, *ARA&A*, 46, 241
- Spina, L., Meléndez, J., Karakas, A. I., et al. 2018, *MNRAS*, 474, 2580
- Spina, L., Nordlander, T., Casey, A. R., et al. 2020, *ApJ*, 895, 52
- Spitoni, E., Silva Aguirre, V., Matteucci, F., Calura, F., & Grisoni, V. 2019, *A&A*, 623, A60
- Sun, W. X., Huang, Y., Wang, H. F., et al. 2020, *ApJ*, 903, 12
- Tautvaišienė, G., Drazdauskas, A., Mikolaitis, Š., et al. 2015, *A&A*, 573, A55
- Tautvaišienė, G., Viscasillas Vázquez, C., Mikolaitis, Š., et al. 2021, *A&A*, 649, A126
- Thompson, T. A., & ud-Doula, A., 2018, *MNRAS*, 476, 5502
- Trevisan, M., & Barbuy, B. 2014, *A&A*, 570, A22
- Vangioni, E., Goriely, S., Daigne, F., François, P., & Belczynski, K. 2016, *MNRAS*, 455, 17
- Viscasillas Vázquez, C., Magrini, L., Casali, G., et al. 2022, *A&A*, 660, A135
- Watson, D., Hansen, C. J., Selsing, J., et al. 2019, *Nature*, 574, 497
- Woolley, S. E., & Weaver, T. A. 1995, *ApJS*, 101, 181
- Woolley, S. E., Wilson, J. R., Mathews, G. J., Hoffman, R. D., & Meyer, B. S. 1994, *ApJ*, 433, 229
- Xing, Q.-F., Zhao, G., Aoki, W., et al. 2019, *Nat. Astron.*, 3, 631
- Zhang, M., Xiang, M., Zhang, H.-W., et al. 2021, *ApJ*, 922, 145

¹ INAF – Osservatorio Astrofisico di Arcetri, Largo E. Fermi 5, 50125 Firenze, Italy
e-mail: mathieu.van+der+swaelmen@inaf.it, laura.magrini@inaf.it

² Institute of Theoretical Physics and Astronomy, Vilnius University, Sauletekio av. 3, 10257 Vilnius, Lithuania

³ Dipartimento di Fisica, Sezione di Astronomia, Università di Trieste, Via G. B. Tiepolo 11, 34143 Trieste, Italy

⁴ INAF, Osservatorio Astronomico di Trieste, Via Tiepolo 11, 34143 Trieste, Italy

⁵ INFN, Sezione di Trieste, Via A. Valerio 2, 34127 Trieste, Italy

⁶ INAF – Osservatorio Astrofisico d’Abruzzo, via Maggini snc, 64100, Teramo, Italy

⁷ INFN – Sezione di Perugia, via A. Pascoli, 06123 Perugia, Italy

⁸ Goethe University Frankfurt, Max-von-Laue-Strasse 1, Frankfurt am Main 60438, Germany

⁹ Lund Observatory, Department of Astronomy and Theoretical Physics, Box 43, 22100 Lund, Sweden

- ¹⁰ Max Planck Institute for Astronomy, Königstuhl 17, 69117 Heidelberg, Germany
- ¹¹ Niels Bohr International Academy, Niels Bohr Institute, University of Copenhagen Blegdamsvej 17, 2100 Copenhagen, Denmark
- ¹² INAF – Osservatorio di Astrofisica e Scienza dello Spazio di Bologna, via Gobetti 93/3, 40129, Bologna, Italy
- ¹³ Departamento de Astrofísica, Centro de Astrobiología (CSIC-INTA), ESAC Campus, Camino Bajo del Castillo s/n, 28692 Villanueva de la Cañada, Madrid, Spain
- ¹⁴ Leibniz-Institut für Astrophysik Potsdam, An der Sternwarte 16, 14482 Potsdam, Germany
- ¹⁵ Department of Physics and Astronomy, Division of Astronomy and Space Physics, Angstrom laboratory, Uppsala University, Box 516, 75120 Uppsala, Sweden
- ¹⁶ Instituto de Astrofísica de Canarias, 38205 La Laguna, Tenerife, Spain
- ¹⁷ Departamento de Astrofísica, Universidad de La Laguna, 38206 La Laguna, Tenerife, Spain
- ¹⁸ Nicolaus Copernicus Astronomical Center, Polish Academy of Sciences, ul. Bartycka 18, 00-716 Warsaw, Poland
- ¹⁹ INAF – Padova Observatory, Vicolo dell’Osservatorio 5, 35122 Padova, Italy

Appendix A: Additional material

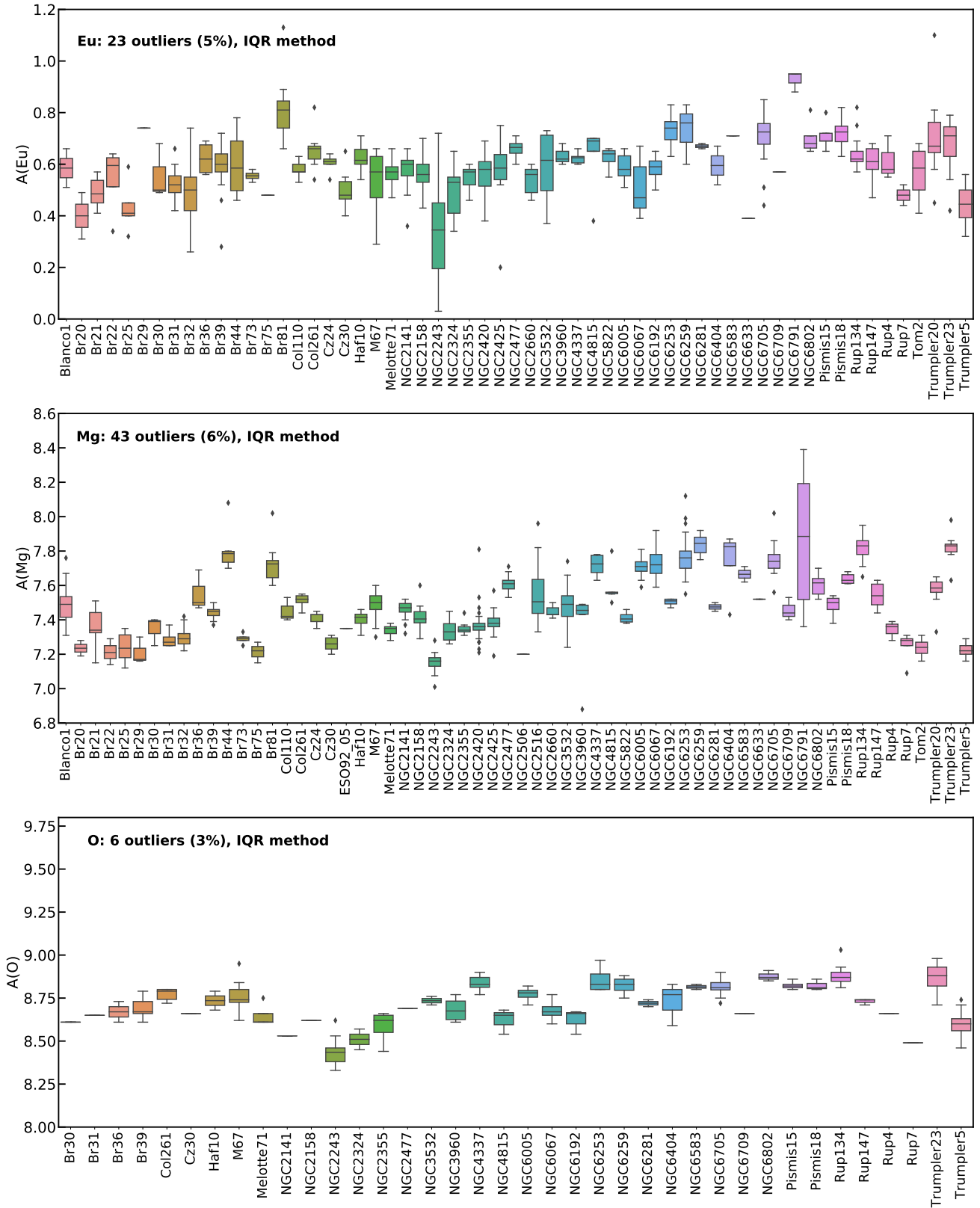


Fig. A.1. Boxplots with the interquartile range of the abundance for each of the clusters with the outliers of Eu, Mg, and O (observations that fall below $Q1 - 1.5 \text{ IQR}$ or above $Q3 + 1.5 \text{ IQR}$).

Table A.1. Average [El/H] and σ [El/H] for our sample of open clusters. The age (Gy) and R_{GC} (kpc) are from Cantat-Gaudin et al. (2020), and the [Fe/H] are from Randich et al. (2022).

GES_FLD	[Fe/H]	age (Gy)	R_{GC} (kpc)	[O I/H]	σ [O I/H]	[Mg I/H]	σ [Mg I/H]	[Mo I/H]	σ [Mo I/H]	[Pr II/H]	σ [Pr II/H]	[Nd II/H]	σ [Nd II/H]	[Eu II/H]	σ [Eu II/H]
Blanco 1	-0.03	0.1	8.3			-0.01	0.1			-0.09	0.11	0.15	0.02	0.05	0.11
Berkeley 20	-0.38	4.79	16.32			-0.29	0.06	-0.16	0.33	-0.31	0.01	-0.14	0.22	-0.16	0.13
Berkeley 21	-0.21	2.14	14.73			-0.17	0.1	-0.24	0.07	-0.11	0.07	0.14	0.1	-0.07	0.06
Berkeley 22	-0.26	2.45	14.29			-0.32	0.08	0.11	0.24	-0.24		0.02	0.14	0.05	0.04
Berkeley 25	-0.25	2.45	13.81			-0.29	0.09	0.03	0.25	-0.15	0.16	0.03	0.1	-0.14	0.03
Berkeley 29	-0.36	3.09	20.58			-0.32	0.08	0.03				-0.02	0.06	0.18	
Berkeley 30	-0.13	0.3	13.25	-0.12		-0.18	0.08	-0.18		0.02	0.09	0.12	0.08	-0.0	0.11
Berkeley 31	-0.31	2.82	15.09	-0.08		-0.24	0.04	-0.12	0.04	-0.15	0.07	-0.02	0.01	-0.05	0.06
Berkeley 32	-0.29	4.9	11.14			-0.24	0.05	-0.15	0.13	-0.17	0.1	-0.09	0.09	-0.08	0.12
Berkeley 36	-0.15	6.76	11.73	-0.06	0.08	-0.02	0.12	-0.19	0.13	0.08		-0.09	0.18	0.06	0.07
Berkeley 39	-0.14	5.62	11.49	-0.04	0.07	-0.08	0.04	-0.09	0.1	-0.02	0.05	0.0	0.05	0.05	0.05
Berkeley 44	0.22	1.45	7.01			0.23	0.04	0.14	0.03	0.23	0.08	0.09	0.1	0.04	0.15
Berkeley 73	-0.26	1.41	13.76			-0.24	0.0	-0.04	0.19	-0.07	0.07	0.12	0.06	-0.01	0.02
Berkeley 75	-0.34	1.7	14.67			-0.32	0.06					0.01	0.19	-0.08	
Berkeley 81	0.22	1.15	5.88			0.16	0.07	0.05	0.08	0.23	0.01	0.25	0.07	0.22	0.07
Collinder 110	-0.1	1.82	10.29			-0.08	0.06	0.11	0.02	0.06	0.04	0.16	0.07	0.02	0.04
Collinder 261	-0.05	6.31	7.26	0.04	0.04	-0.02	0.04	-0.04	0.02	0.03	0.13	-0.01	0.02	0.09	0.03
Czernik 24	-0.11	2.69	12.29			-0.12	0.04	0.05	0.08	0.03	0.01	0.22	0.06	0.06	0.02
Czernik 30	-0.31	2.88	13.78	-0.07		-0.27	0.04	-0.07	0.28	-0.07	0.02	-0.04	0.05	-0.09	0.05
ESO92_05	-0.29	4.47	12.82			-0.18		0.26				0.04			
Haffner 10	-0.1	3.8	10.82	0.0	0.08	-0.13	0.04	0.0	0.11	0.02	0.04	0.16	0.08	0.07	0.05
M67	0.0	4.27	8.96	-0.0	0.06	0.0	0.05	-0.0	0.09	0.0	0.07	0.0	0.06	-0.0	0.11
Melotte71	-0.15	0.98	9.87	-0.11	0.03	-0.19	0.03			0.02	0.04	0.07	0.03	0.0	0.06
NGC2141	-0.04	1.86	13.34	-0.2		-0.06	0.03	0.04	0.12	0.06	0.04	0.13	0.12	0.03	0.05
NGC2158	-0.15	1.55	12.62	-0.11		-0.12	0.05	0.04	0.09	0.02	0.05	0.15	0.06	0.0	0.07
NGC2243	-0.45	4.37	10.58	-0.31	0.06	-0.37	0.04	-0.31	0.05	-0.38	0.08	-0.14	0.17	-0.22	0.19
NGC2324	-0.18	0.54	12.08	-0.22	0.08	-0.18	0.08	-0.1	0.06	-0.04	0.09	0.02	0.05	-0.06	0.12
NGC2355	-0.13	1.0	10.11	-0.14	0.08	-0.19	0.02	0.01	0.1	0.03	0.05	0.09	0.06	-0.01	0.05
NGC2420	-0.15	1.74	10.68			-0.15	0.04	-0.06	0.11	-0.01	0.06	0.1	0.07	0.0	0.08
NGC2425	-0.12	2.4	10.92			-0.15	0.05	-0.03	0.14	0.02	0.05	0.13	0.06	0.04	0.07
NGC2477	0.14	1.12	8.85	-0.04		0.09	0.06	0.21	0.02	0.15	0.05	0.15	0.02	0.1	0.04
NGC2506	-0.34	1.66	10.62			-0.33									
NGC2516	-0.04	0.24	8.32			0.02	0.11					0.45	0.08		
NGC2660	-0.05	0.93	8.98			-0.08	0.04	0.01		0.12	0.04	0.13	0.03	-0.02	0.06
NGC3532	-0.03	0.4	8.19	0.0	0.04	-0.01	0.09	0.06	0.08	0.07	0.12	0.27	0.16	0.05	0.13
NGC3960	0.0	0.87	7.68	-0.05	0.08	-0.07	0.03	0.12	0.01	0.14	0.01	0.17	0.01	0.07	0.03
NGC4337	0.24	1.45	7.45	0.11	0.05	0.19	0.06	0.13	0.03	0.14	0.03	0.11	0.03	0.06	0.02
NGC4815	0.08	0.37	7.07	-0.11	0.07	0.03	0.0	0.06	0.12	0.08	0.02	0.18	0.02	0.12	0.02
NGC5822	0.02	0.91	7.69			-0.12	0.04	0.07	0.02	0.05	0.07	0.12	0.02	0.06	0.05
NGC6005	0.22	1.26	6.51	0.04	0.03	0.19	0.05	0.1	0.04	0.12	0.01	0.09	0.05	0.03	0.05
NGC6067	0.03	0.13	6.78	-0.05	0.06	0.21	0.1	0.12	0.08	0.01	0.03	-0.0	0.06	-0.05	0.12
NGC6192	-0.08	0.24	6.73	-0.11	0.07	-0.03	0.02	0.07	0.07	0.01	0.09	0.07	0.09	0.02	0.06
NGC6253	0.34	3.24	6.88	0.13	0.07	0.26	0.06	0.18	0.06	0.21	0.03	0.45	0.24	0.17	0.05
NGC6259	0.18	0.27	6.18	0.09	0.05	0.3	0.06	0.18	0.07	0.14	0.07	0.13	0.05	0.18	0.07
NGC6281	-0.04	0.51	7.81	-0.01	0.03	-0.06	0.04	0.07	0.04	0.08	0.01	0.15	0.04	0.11	0.01
NGC6404	0.01	0.1	5.85	-0.0	0.12	0.31	0.03	0.04	0.21	0.05		-0.04	0.07	0.03	0.11
NGC6583	0.22	1.2	6.32	0.08	0.02	0.13	0.06	-0.01	0.06			0.05	0.03	0.15	
NGC6633	-0.03	0.69	8.0			0.04						0.27	0.18	-0.14	
NGC6705	0.03	0.31	6.46	0.09	0.04	0.21	0.05	0.12	0.09	0.08	0.03	0.05	0.07	0.17	0.06
NGC6709	-0.02	0.19	7.6	-0.07		-0.04	0.04	-0.01		0.0		0.37	0.31	0.01	
NGC6791	0.22	6.31	7.94			0.35	0.44	0.67	0.51	0.27	0.16	0.19	0.32	0.37	0.04
NGC6802	0.14	0.66	7.14	0.15	0.03	0.07	0.06	0.16	0.05	0.16	0.01	0.25	0.08	0.12	0.03
Pismis 15	0.02	0.87	8.62	0.09	0.02	-0.05	0.06	0.11	0.13	0.17	0.07	0.28	0.1	0.13	0.03
Pismis 18	0.14	0.58	6.94	0.09	0.03	0.11	0.03	0.11	0.07	0.14	0.03	0.16	0.04	0.16	0.06
Ruprecht 134	0.27	1.66	6.09	0.14	0.04	0.3	0.06	0.18	0.05	0.16	0.05	0.11	0.04	0.06	0.03
Ruprecht 147	0.12	3.02	8.05	-0.07	0.02	0.06	0.08					-0.01	0.04	0.07	0.08
Ruprecht 4	-0.13	0.85	11.68	-0.07		-0.19	0.06			0.09	0.05	0.14	0.02	0.05	0.09
Ruprecht 7	-0.24	0.23	13.11	-0.24		-0.25	0.02			-0.07	0.01	0.09	0.06	-0.08	0.04
Tombaugh 2	-0.24	1.62	15.76			-0.29	0.05	-0.32		-0.01	0.09	0.07	0.04	0.0	0.12
Trumpler 20	0.13	1.86	7.18			0.06	0.04	0.11	0.08	0.13	0.05	0.18	0.05	0.13	0.07
Trumpler 23	0.2	0.71	6.27	0.13	0.09	0.29	0.03	0.14	0.04	0.15	0.03	0.11	0.02	0.13	0.08
Trumpler 5	-0.35	4.27	11.21	-0.14	0.07	-0.31	0.03	-0.14	0.08	-0.2	0.1	-0.04	0.08	-0.12	0.07

Table A.2. Average [El/Fe] and σ [El/Fe] for our sample of open clusters. The age (Gyr) and R_{GC} (kpc) are from Cantat-Gaudin et al. (2020), and the [Fe/H] are from Randich et al. (2022).

GES_FLD	[Fe/H]	Age (Gyr)	R_{GC} (kpc)	[O I/Fe]	σ [O I/Fe]	[Mg I/Fe]	σ [Mg I/Fe]	[Mo I/Fe]	σ [Mo I/Fe]	[Pr II/Fe]	σ [Pr II/Fe]	[Nd II/Fe]	σ [Nd II/Fe]	[Eu II/Fe]	σ [Eu II/Fe]
Blanco 1	-0.03	0.1	8.3			0.02	0.06			-0.06	0.15	0.19	0.03	0.06	0.08
Berkeley 20	-0.38	4.79	16.32			0.08	0.01	0.22	0.25	0.07	0.07	0.23	0.14	0.21	0.05
Berkeley 21	-0.21	2.14	14.73			0.03	0.08	-0.01	0.07	0.12	0.05	0.35	0.07	0.16	0.05
Berkeley 22	-0.26	2.45	14.29			-0.01	0.15	0.41	0.19	0.14		0.28	0.12	0.29	0.05
Berkeley 25	-0.25	2.45	13.81			0.01	0.04	0.34	0.11	0.18	0.03	0.32	0.09	0.17	0.02
Berkeley 29	-0.36	3.09	20.58			0.07	0.11	0.47				0.4	0.09	0.58	
Berkeley 30	-0.13	0.3	13.25	0.05		-0.04	0.09	-0.01		0.16	0.08	0.27	0.06	0.14	0.09
Berkeley 31	-0.31	2.82	15.09	0.22		0.04	0.06	0.21	0.04	0.17	0.05	0.3	0.03	0.27	0.06
Berkeley 32	-0.29	4.9	11.14			0.05	0.06	0.15	0.1	0.12	0.06	0.2	0.06	0.2	0.08
Berkeley 36	-0.15	6.76	11.73	0.2	0.03	0.18	0.11	0.03	0.13	0.23		0.15	0.1	0.21	0.07
Berkeley 39	-0.14	5.62	11.49	0.12	0.05	0.06	0.06	0.04	0.1	0.13	0.05	0.14	0.05	0.19	0.04
Berkeley 44	0.22	1.45	7.01			0.02	0.11	-0.06	0.06	-0.01	0.17	-0.08	0.14	-0.12	0.1
Berkeley 73	-0.26	1.41	13.76			0.01	0.01	0.22	0.15	0.19	0.08	0.38	0.07	0.25	0.05
Berkeley 75	-0.34	1.7	14.67			0.03	0.08			0.09		0.36	0.13	0.31	
Berkeley 81	0.22	1.15	5.88			-0.05	0.11	-0.17	0.1	-0.01	0.06	0.04	0.09	0.02	0.11
Collinder 110	-0.1	1.82	10.29			0.02	0.09	0.21	0.06	0.15	0.03	0.26	0.09	0.12	0.04
Collinder 261	-0.05	6.31	7.26	0.09	0.09	0.03	0.08	0.0	0.09	0.08	0.07	0.07	0.04	0.16	0.05
Czernik 24	-0.11	2.69	12.29			-0.01	0.07	0.2	0.04	0.14	0.05	0.33	0.04	0.17	0.03
Czernik 30	-0.31	2.88	13.78	0.25		0.06	0.04	0.28	0.31	0.25	0.02	0.29	0.05	0.24	0.06
ESO92_05	-0.29	4.47	12.82			0.21		0.53				0.31			
Haffner 10	-0.1	3.8	10.82	0.12	0.11	-0.01	0.04	0.11	0.11	0.14	0.05	0.27	0.06	0.18	0.06
M67	0.0	4.27	8.96	0.01	0.06	0.02	0.04	0.01	0.09	0.0	0.06	0.02	0.05	0.01	0.1
Melotte71	-0.15	0.98	9.87	0.0	0.03	-0.04	0.11			0.15	0.04	0.24	0.1	0.16	0.11
NGC2141	-0.04	1.86	13.34	-0.02		-0.02	0.04	0.11	0.11	0.09	0.05	0.2	0.07	0.07	0.05
NGC2158	-0.15	1.55	12.62	0.09		0.04	0.04	0.19	0.07	0.18	0.04	0.31	0.03	0.17	0.05
NGC2243	-0.45	4.37	10.58	0.17	0.06	0.1	0.06	0.15	0.07	0.1	0.08	0.31	0.13	0.26	0.17
NGC2324	-0.18	0.54	12.08	-0.04	0.08	-0.01	0.07	0.08	0.06	0.14	0.09	0.2	0.05	0.12	0.12
NGC2355	-0.13	1.0	10.11	-0.03	0.05	-0.09	0.04	0.14	0.08	0.13	0.05	0.2	0.04	0.09	0.05
NGC2420	-0.15	1.74	10.68			0.02	0.08	0.1	0.1	0.14	0.05	0.27	0.09	0.16	0.08
NGC2425	-0.12	2.4	10.92			0.01	0.08	0.11	0.12	0.17	0.04	0.23	0.08	0.15	0.07
NGC2477	0.14	1.12	8.85	-0.14		-0.05	0.03	0.1	0.02	0.05	0.07	0.03	0.02	-0.01	0.05
NGC2506	-0.34	1.66	10.62			0.01									
NGC2516	-0.04	0.24	8.32			0.06	0.07					0.51	0.13		
NGC2660	-0.05	0.93	8.98			-0.03	0.02	0.09		0.16	0.02	0.2	0.02	0.03	0.05
NGC3532	-0.03	0.4	8.19	-0.02	0.01	-0.0	0.09	0.03	0.08	0.07	0.09	0.27	0.16	0.06	0.11
NGC3960	0.0	0.87	7.68	-0.05	0.06	-0.07	0.03	0.12	0.01	0.13	0.01	0.16	0.01	0.07	0.02
NGC4337	0.24	1.45	7.45	-0.15	0.04	-0.07	0.08	-0.12	0.03	-0.11	0.02	-0.14	0.02	-0.19	0.03
NGC4815	0.08	0.37	7.07	-0.07	0.03	0.03	0.07	0.06	0.07	0.06	0.03	0.18	0.02	0.11	0.04
NGC5822	0.02	0.91	7.69			-0.13	0.02	0.05	0.01	0.05	0.05	0.11	0.02	0.05	0.03
NGC6005	0.22	1.26	6.51	-0.17	0.06	-0.03	0.05	-0.12	0.06	-0.12	0.02	-0.12	0.06	-0.19	0.06
NGC6067	0.03	0.13	6.78	-0.02	0.09	0.19	0.14	0.09	0.12	-0.01	0.12	0.02	0.09	-0.02	0.15
NGC6192	-0.08	0.24	6.73	-0.04	0.02	0.06	0.08	0.13	0.06	0.1	0.04	0.16	0.04	0.11	0.06
NGC6253	0.34	3.24	6.88	-0.13	0.09	-0.08	0.07	-0.08	0.1	-0.04	0.06	0.11	0.2	-0.08	0.09
NGC6259	0.18	0.27	6.18	-0.11	0.05	0.13	0.07	0.0	0.05	-0.03	0.07	-0.06	0.05	0.01	0.09
NGC6281	-0.04	0.51	7.81	0.03	0.02	-0.01	0.01	0.12	0.01	0.12	0.06	0.19	0.01	0.15	0.06
NGC6404	0.01	0.1	5.85	0.05	0.03	0.34	0.13	0.15	0.11	-0.02		0.03	0.07	0.02	0.02
NGC6583	0.22	1.2	6.32	-0.14	0.01	-0.09	0.05	-0.23	0.05			-0.17	0.01	-0.06	
NGC6633	-0.03	0.69	8.0			0.03						0.34	0.29	-0.15	
NGC6705	0.03	0.31	6.46	0.05	0.06	0.18	0.08	0.09	0.13	0.05	0.05	0.02	0.09	0.13	0.09
NGC6709	-0.02	0.19	7.6	-0.0		-0.0	0.06	0.06		0.07		0.42	0.28	0.08	
NGC6791	0.22	6.31	7.94			0.2	0.35	0.61	0.32	-0.0	0.17	0.11	0.1	0.28	0.03
NGC6802	0.14	0.66	7.14	-0.01	0.04	-0.06	0.08	0.02	0.06	0.03	0.03	0.11	0.06	-0.02	0.05
Pismis 15	0.02	0.87	8.62	0.05	0.02	-0.07	0.02	0.11	0.11	0.13	0.04	0.24	0.08	0.09	0.05
Pismis 18	0.14	0.58	6.94	-0.07	0.02	-0.04	0.03	-0.04	0.05	-0.02	0.07	0.02	0.02	0.02	0.09
Ruprecht 134	0.27	1.66	6.09	-0.12	0.07	0.02	0.06	-0.09	0.07	-0.11	0.05	-0.17	0.04	-0.2	0.04
Ruprecht 147	0.12	3.02	8.05	-0.2	0.02	-0.06	0.06					-0.13	0.03	-0.04	0.09
Ruprecht 4	-0.13	0.85	11.68	0.05		-0.05	0.06			0.22	0.04	0.27	0.03	0.19	0.07
Ruprecht 7	-0.24	0.23	13.11	-0.05		-0.02	0.03			0.18	0.08	0.33	0.09	0.14	0.07
Tombaugh 2	-0.24	1.62	15.76			-0.06	0.08	-0.06		0.19	0.03	0.32	0.07	0.24	0.07
Trumpler 20	0.13	1.86	7.18			-0.07	0.04	-0.01	0.08	0.0	0.06	0.06	0.06	0.01	0.1
Trumpler 23	0.2	0.71	6.27	-0.08	0.09	0.08	0.04	-0.07	0.06	-0.07	0.05	-0.1	0.03	-0.08	0.09
Trumpler 5	-0.35	4.27	11.21	0.21	0.06	0.04	0.03	0.2	0.07	0.15	0.1	0.31	0.07	0.23	0.07

Table A.3. 23 member stars with values of $A(\text{Eu})$ enhanced or decreased and classified as outliers in their respective open clusters according to the IQR method.

CNAME	GES_FLD	A(Eu)
05582595+0746114	Berkeley 22	0.34
06411680-1630203	Berkeley 25	0.59
06412105-1629038	Berkeley 25	0.32
06573668+0810127	Berkeley 31	0.66
07464760-0439563	Berkeley 39	0.28
07464911-0441557	Berkeley 39	0.46
19013651-0027021	Berkeley 81	1.13
12381233-6820314	Collinder 261	0.54
12381261-6821494	Collinder 261	0.82
05552710+2052163	Czernik 24	0.54
07310960-0957183	Czernik 30	0.65
06025078+1030280	NGC2141	0.36
07382342-1453123	NGC2425	0.2
12572442-6455173	NGC4815	0.38
18504737-0617184	NGC6705	0.51
18511116-0614340	NGC6705	0.44
19303309+2015442	NGC6802	0.81
09345191-4800467	Pismis15	0.8
17523054-2930564	Ruprecht 134	0.75
17524742-2931471	Ruprecht 134	0.82
12390476-6041475	Trumpler20	1.1
12391113-6036528	Trumpler20	0.45
16004035-5333047	Trumpler23	0.42